CentraleSupélec

UNIVERSIDAD
DE CANTABRIA

Instituto de Física de Cantabria
Santander, Spain

Polarization Dynamics of Vertical-Cavity Surface-Emitting Lasers (VCSELs) subject to parallel optical injection

Final year trainee report
CentraleSupélec & University of Lorraine
Major Photonics

Autor : Florian Denis
Director : Angel Valle Gutiérez
Supervisor : Marc Sciamanna

April - September 2016

Abstract

In this work, we investigate the polarization dynamics of vertical-cavity surface-emitting lasers (VCSELs) subject to parallel optical injection.

We investigate theoretically and experimentally the polarization switching found in a transverse mode VCSEL subject to parallel optical injection. More specifically we focus on a recently found state of simultaneous injection locking of the parallel polarization and excitation of the orthogonal polarization of the solitary device, termed IL+PS. Simple mathematical expressions resulting from the spin-flip model and describing this state are found.

Numerical simulations of the spin-flip model and stability analysis of the steady state describing the IL+PS state are performed to identify the region of the injected power-frequency detuning plane where this solution is stable. Experimental mapping of this region is presented. Bistability induced by power variation of the master laser is also studied, numerically, theoretically and experimentally. Very good agreement is found, both qualitatively and quantitatively.

We present an experimental mapping of the non-linear dynamics of the VCSEL subject to parallel optical injection. States that have been widely explored and studied are found, along with new states of simultaneous non-linear excitation of both polarizations. Fixed points in both polarizations (IL+PS), limit cycle in both polarizations, period doubling in both polarizations, chaotic behaviour in both polarizations are observed and mapped for several bias currents. We also find behaviours resulting from an aperiodic switching between two stable non-linear states.

Finally, we explore the hopping dynamics found in the VCSEL when subject to parallel optical injection. These hopping dynamics present heavy tails residence time distributions, and a spectral analysis shows a 1/f noise hopping mechanism. Work on this subject is still in progress.

Keywords : VCSEL, polarization switching, non-linear dynamics, optical injection, injection locking

Contents

List of Tables

List of Figures

Introduction

Vertical-Cavity Surface-Emitting Lasers (VCSELs) have attracted considerable interest for many years. Indeed, this semiconductor laser (SL) offers many advantages in comparison with edge-emitting devices - that have been widely explored [1, 2] - including high coupling efficiency to optical fibres, low threshold current and power consumption, high energy efficiency, low fabrication costs, compactness and ease of 2D array packaging, on-wafer testing capability, etc... VCSELs also operate as single-longitudinal mode devices, but show complex polarization properties [2]. When lasing in their fundamental mode, the VCSEL usually emits light alongside one of its two orthogonally polarized linear modes. A polarization side mode suppression ratio is defined as the power ratio between the two polarization modes. This ratio depends on the temperature and the bias current, and polarization switching (PS) can be observed when changing these two parameters [3–5].

The inherent properties and advantages of VCSELs make them good candidates for use in all-optical telecommunication networks. But they become excellent candidates when improving some of their other properties, that can be done through optical injection (OI). OI in semiconductor lasers is a well known technique of improvement of laser diode performances without modifying the semiconductor design [6], usually through the injection locking (IL) phenomenon. This way of performance improvement has been explore for VCSELs [7] and has given good results in terms of modulation bandwidth enhancement, chirp reduction and non-linearities reduction. Also PS can be attained through optical injection [8–11].

Polarization switching performed through optical injection is usually attained with orthogonal optical injection, that is injecting linearly polarized light along the suppressed mode of the free-running VCSEL [8–11]. However, PS has been obtained very recently by performing parallel optical injection [12]. In this paper was described a state, named IL+PS, in which the parallel polarization is locked on the injected light, and the orthogonal polarization of the free-running VCSEL is simultaneously excited. This state is unusual because optical injection along the emitting polarization mode result in an excitation of the suppressed mode of the solitary VCSEL. This work focus on the characterization of this IL+PS state.

Bistability in laser diodes (see [13] and references therein) and in VCSEL [14, 15] has also been the subject to a large amount of studies, mostly in view of all-optical signal processing. It has been demonstrated that bistable VCSEL can be used as all-optical memory [16], or to perform all-optical shift register [17] and all-optical flip-flop operations [18, 19]. The IL+PS state that has been described previously and is presented in [12] present bistable properties that will be explored in the present work

VCSELs, as well as semiconductor lasers, subject to optical injection can present a large variety of non-linear dynamics, as limit cycles, period doubling, and chaotic behaviours. These non-linear dynamics are usually avoided in all-optical signal transmission, however their understanding is necessary and has been the subject of a large amount of studies in the last decades [20–23]. Both experimental and theoretical studies of these non-linear behaviours show that most of these behaviours are subject to bistability, or multistability. In this context, the initial conditions of the system are of importance, but noise also plays an important role, and can induce attractor hopping [24,25], coherence resonance [26,27], etc.

This work mainly focuses on the IL+PS state described in [12] found on the VCSEL subject to parallel optical injection. We perform numerical simulations of the spin-flip model in order to map in the injected power-frequency detuning plane the region where this state is stable. Bistability is also explored numerically. We perform a linear stability analysis based on the work from Friart *et al.* [28] that we adapt to our system. This stability analysis give the theoretical maps of stability of the IL+PS state. Experimental mapping of the IL+PS state is also performed for several bias currents, as well as a mapping of all the non-linear behaviours of the VCSEL subject to parallel optical injection. Non-linear behaviours in which only the parallel polarization or both polarizations are involved are found (as periodic solutions, chaotic states, periodic behaviours in both polarizations...), and finally we found a region where attractor hopping dynamics can be observed.

This document is organized as follows. In a first section we present some theoretical background on semiconductor lasers, VCSELs, optical injection, and we present the spin-flip model that gives simple equations to describe the IL+PS state. In a second chapter, we perform linear stability analysis and we perform numerical simulations of the spin-flip model in order to describe and map the IL+PS region. In a third section of this report, we present the experimental setup used to attain parallel optical injection, we describe the experimental equipment, and we present the experimental results with regard to the mapping of the IL+PS region, the measurement of a parameter - the linear dichroism - of the VCSEL, the bistability properties of the IL+PS region, and the complete mapping of the polarization non-linear dynamics of the VCSEL subject to parallel optical injection. The different states are described in term of spectra and times series. Finally, in a last chapter, we present some results, that are still in progress, about attractor hopping dynamics, coherence resonance and 1/f noise induced by this kind of hopping. Appendix can be found after a summary, and are presented the mathematical steps of long calculations (steady state of the IL+PS state, variable change, stability analysis), a quick and qualitative presentation of the delayed bifurcation theory, and the list of submitted manuscripts resulting from this work.

1 Theoretical Background

In this chapter, we give the theoretical concepts and models that are relevant for the following chapters. First an introduction about Surface-Emitting Vertical-Cavity Lasers (VCSELs) is given. Then we give some basics about optical injection, and finally we explain the Spin-Flip Model that give the equations we will use in the following chapters.

1.1 VCSEL

Here are given some knowledge about VCSELs. Fist we introduce the Semiconductor Laser before going into details about the structure and the characteristics of a VCSEL.

1.1.1 Semiconductor Laser

While the theoretical foundation for the Laser (Light Amplification by Stimulated Emission of Radiations) has been established since 1917 by Albert Einstein and his studies about stimulated emission and population inversion, the first functioning laser only appears with Theodore Maiman in 1960 [29]. The most used type of laser is the semiconductor laser.

There are three possible interactions between matter and radiations. Absorption, spontaneous emission and stimulated emission. Semiconductor lasers operate under stimulated emission (figure 1.1(a)) in a gain medium. More specifically, the stimulated emission is a light-matter interaction between a photon ($h\nu$) and an excited electron of the conduction band (CB). The interaction leads to a down-conversion of the excited electron, which leads to the emission of a clone photon ($h\nu$). The new photon can now interact with other electrons, which leads to the amplification of the figure 1.1(b). This amplification is however only possible if there is a sufficient amount of excited electrons. This phenomenon is the population inversion, maintained by a pump source.

(a) Stimulated Emission (b) Amplification

Figure 1.1: Key processes for semiconductor lasers. Figure (a) shows the process of stimulated emission, and figure (b) shows the amplification phenomenon

Semiconductor lasers are used in any fields thanks to both the size of a semiconductor laser, the amount of light power it can display, and their extremely fast response. One of the main field of application is high speed telecommunications on optical fiber, and many researches are done in the aim of all-optical data transmissions.

There are two types of semiconductor lasers, depending of the direction of the light beam : edge emitting lasers and vertical emitters, which active layer is orthogonal to the light beam. We will focus this document on VCSELs.

1.1.2 Structure of a VCSEL

We will discuss in this section about the structure of a Vertical-Cavity Surface-Emitting Laser, that is given in figure 1.2. To summarize, the active layer (a heterostructured *pn* junction) is orthogonal to the light beam. Thus the length of the cavity is really small (on the order of 1 μm, according to [2]. This heterostructure is thereby between two Bragg reflectors, that allow a sufficiently large gain in the active layer.

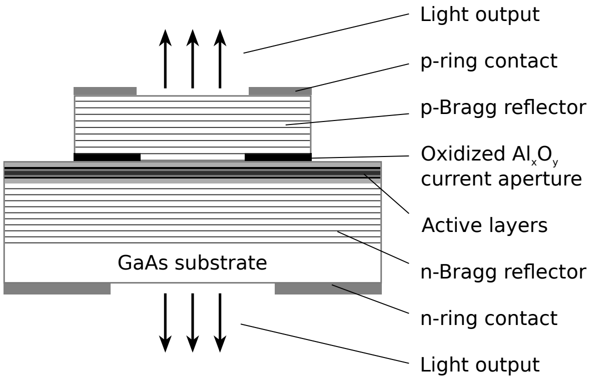

Figure 1.2: Schematic cross-sectional view of a VCSEL, according to [2]

According to [2] describing a 850 nm-wavelength VCSEL, the active layers is usually InGaAs, Bragg reflectors can be pairs of GaAs-AlGaAs or GaAs-AlAs and the substrate is usually made of GaAs. On this work, we focus on long-wavelength VCSEL (1550 nm) for which the active layers are InAlGaAs quantum wells and the Bragg reflectors are pairs of InAlAs-AnAlGaAs [30].

The small size of the cavity leads to two benefits. First, the complete device can be as small as few μm, and secondly the small cavity promote single longitudinal mode devices, even if VCSELs can be multi-mode. Indeed, several transverse modes can be excited, specially for large diameter devices. The VCSEL we focus on has the two orthogonal fundamental transverse mode we will call "parallel", and "orthogonal" shifted 0.26 nm with a side mode suppression ratio of 34 dB according to [12].

1.1.3 Characteristics

We give in this section different characteristics of a VCSEL. The standard rate equation model is given, according to [31] and [32]. These equations (1.1) and (1.2) are the same as the one for a linearly polarized single-mode semiconductor laser.

$$\frac{\mathrm{d}P}{\mathrm{d}t} = G_N(N - N_t)P - \frac{P}{\tau_P} + R_{sp}(N) \tag{1.1}$$

$$\frac{\mathrm{d}N}{\mathrm{d}t} = \frac{I}{e} - R(N) - G_N(N - N_t)P \tag{1.2}$$

In these equations, N is the number of carriers in the active layer, P is the number of photons in the cavity, G_N is the differential gain, N_t is the number of carriers at transparency, τ_p is the photon lifetime, I is the bias current, e the electron charge, and *R(N)* and $R_{sp}(N)$ are two functions representing respectively the carrier recombination rate and the spontaneous emission rate coupled to the laser mode. More informations about those two functions can be found in reference [31].

We can point out the fact that we will not use these equations in the following sections. We will use those given by the Spin-Flip model (see section 1.3), but these equations can give us information about VCSEL characteristics.

One of the main characteristics we can derive from equations (1.1) and (1.2) are the relaxation oscillation frequency ν_R and the damping rate Γ_R, given respectively in (1.3) and (1.4), according to [31]. The relaxation oscillation frequency is a really important parameter and is a limiting factor for the modulation speed, and of the bandwidth for optical data transmissions.

$$\nu_R = \sqrt{\frac{G_N}{e}(I - I_{th})} \tag{1.3}$$

$$\Gamma_R = \frac{1}{2}\left(\frac{1}{\tau_n} + \frac{G_N \tau_p}{e}(I - I_{th})\right) \tag{1.4}$$

In these equations, I_{th} is the threshold current, and τ_n is the differential carrier lifetime at the lasing threshold. The physical explanation of these oscillations is similar to a predator-prey system between photons and active carriers in the cavity.

We can give the theoretical equation for the optical power emitted by a laser, according to [32]. This power is derived from the steady state of equations (1.1) and (1.2). Once again, the expression given in equation (1.5) is not the value we will use in the following sections. We will give another expression, derived from the Spin-Flip model (section 1.3).

$$\mathscr{P} = \eta \frac{h\nu}{e}(I - I_{th}) \tag{1.5}$$

This expression demonstrates that the optical power is proportional to the number of photons above threshold. η is the internal differential quantum efficiency, h is the Plank constant and ν is the emitting frequency of the laser.

1.2 Optical Injection

In this document, we explore the dynamics of VCSELs subject to parallel optical injection. Thus we give in this section some theoretical background about optical injection, in a first part some general concepts, and in a second part we focus on parallel injection.

1.2.1 General concepts

Semiconductors in general and more specifically VCSELs can be subject to optical injection from a master laser, as shown in figure 1.3. The key parameters that allow semiconductors to be sensitive to optical injection are the high gain features, the low facet reflectivity and the amplitude-phase coupling (see α-parameter).

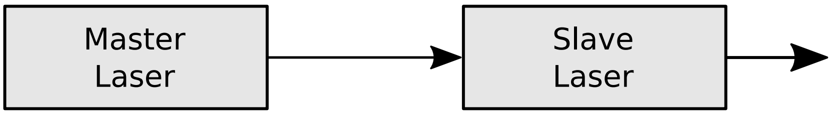

Figure 1.3: Optical injection system in semiconductor lasers, according to [33]

Optical injection has been well studied in regard to the simple dynamics of optical injection locking. However, according to [33], polarized optical injection can leads to various dynamics like four-wave mixing, period-doubling, chaotic behaviour. And more recently the work about parallel optical injection and polarization switching [12], [32] and [21], work that we continue in this document.

More specifically, the light from the master laser is fed into the active layer of the slave laser. we define two parameters that define the optical injection. The frequency detuning ν_i is the difference of frequency between the two free running devices, and the injected power P_{inj} is the power of the master laser. The usual values for the detuning are of the order of several GHz.

When the detuning is of the order of several GHz, and the injected power is large enough, we have a phenomenon of synchronisation of oscillators and we enter in an injection locking dynamic, see [33]. This state leads to a stabilisation of the semiconductor laser, and is really useful in that way.

More recently, studies have shown that optical injection can be polarization selective. Our VCSEL, and most of the VCSELs have two linear polarization modes. One is dominant in the free running state, and we call this direction parallel, or x, and the other one orthogonal, or y. In the following, we use the two terminologies. Orthogonal polarized injection has been well studied [22], and in this work, we continue the study of the dynamics induced by parallel injection [12] [32].

1.2.2 Parallel Optical Injection

This work focus on parallel optical injection. We give here in figure 1.4 a schematic example of parallel optical injection. The injected light polarization is parallel to the dominant polarization of the free running VCSEL.

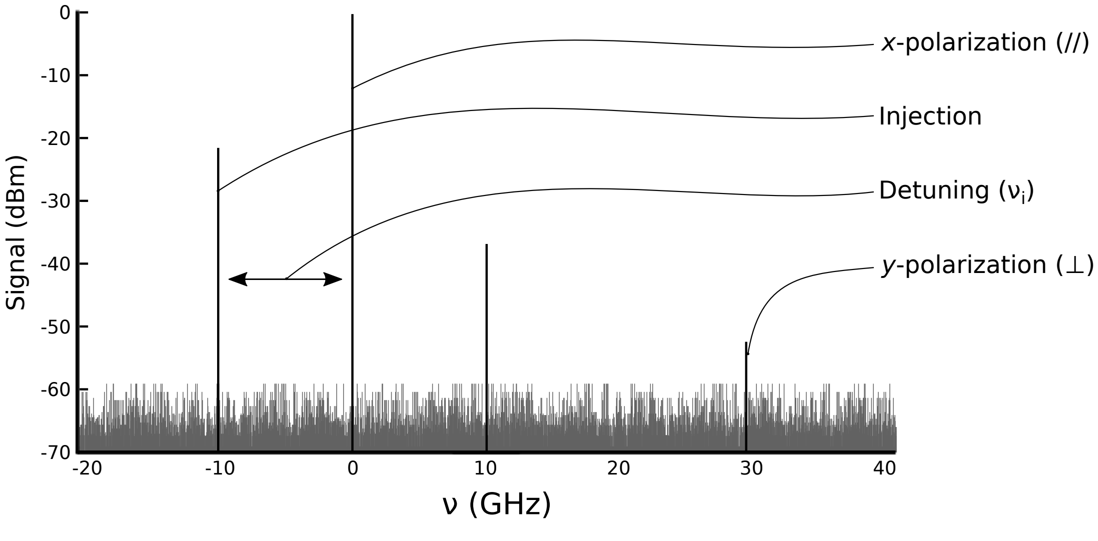

Figure 1.4: Parallel optical injection in a VCSEL, parallel polarization dominant, injection and detuning

We will see in the section 1.3 about Spin-Flip model how to describe each polarization field mathematically, and how to add the injection in the equations according to [12]. Then in the following sections, we will study the new dynamical states that appear when changing the two key parameters of the injection ν_i and P_{inj}, continuing the works [12] and [32].

1.3 Spin-Flip Model & Rate Equations

In this section, we develop a model, the Spin-Flip Model, that will allow us to describe more efficiently the rate equations, taking into account the expressions for the parallel and the orthogonal fields.

1.3.1 Spin-Flip Model (SFM)

The Spin-Flip model, as described in [3], is a four-level model. This four-level model for polarization dynamics of quantum well lasers is given in figure 1.5 and takes into account the degeneracy removal between angular momentum ±1/2 and ±3/2 due to the quantum confinement.

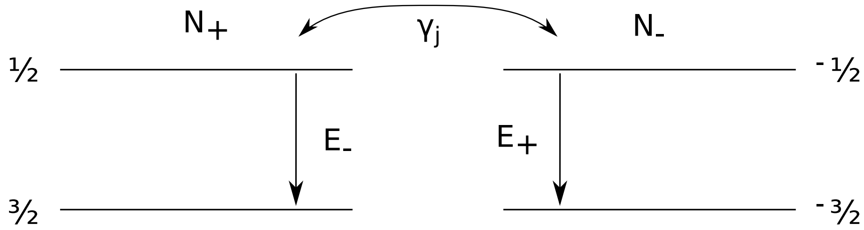

Figure 1.5: Spin Flip Model - Band Structure of a Quantum Well, according to [3]

As explained in [3], the model separates the carriers that leads to the two TE (transverse electric) modes of the field N_+ and N_- (with a decay rate γ_j accounting for the mixing of populations), and give the dynamical equations for the two TE modes of the field (equations (1.6) and (1.7)) and two new functions : $D = (N_+ + N_-)/2$ and $n = (N_+ - N_-)/2$ (equations (1.8) and (1.9)).

D is the total population inversion and n is the difference between population inversion for the spin-up and the spin-down channels.

$$\frac{\mathrm{d}E_x}{\mathrm{d}t} = -(\kappa + \gamma_a)E_x - i(\kappa\alpha + \gamma_p)E_x + \kappa(1 + i\alpha)(DE_x + inE_y) \tag{1.6}$$

$$\frac{\mathrm{d}E_y}{\mathrm{d}t} = -(\kappa - \gamma_a)E_y - i(\kappa\alpha - \gamma_p)E_y + \kappa(1 + i\alpha)(DE_y - inE_x) \tag{1.7}$$

$$\frac{\mathrm{d}D}{\mathrm{d}t} = -\gamma\left[D(1 + |E_x|^2 + |E_y|^2) - \mu + in(E_yE_x^* - E_xE_y^*)\right] \tag{1.8}$$

$$\frac{\mathrm{d}n}{\mathrm{d}t} = -\gamma_s n - \gamma\left[n(|E_x|^2 + |E_y|^2) + iD(E_yE_x^* - E_xE_y^*)\right] \tag{1.9}$$

In these equations, κ is the field decay rate, γ_a is the linear dichroism, α is the linewidth enhancement factor, γ_p is the linear birefringence, γ is the decay rate of D, γ_s is the spin-flip relaxation rate and μ is the normalized bias current.

1.3.2 Parallel Optical Injection

Equations (1.6) to (1.9) do not take into account the optical injection. While the injection is only on the x mode polarization, the optical injection term is easy to add to the model. The equation for the x-polarization field needs to be substituted by (1.10).

$$\frac{\mathrm{d}E_x}{\mathrm{d}t} = -(\kappa+\gamma_a)E_x - i(\kappa\alpha+\gamma_p)E_x + \kappa(1+i\alpha)(DE_x + inE_y) + \kappa E_{inj}e^{i2\pi\nu_{inj}t} \tag{1.10}$$

In this equation, E_{inj} is the amplitude of the injected light and ν_{inj} is a detuning between the frequency of injection and an intermediate frequency we define in 1.3.3.

1.3.3 Simplifications & Steady state

In this section, we give a simple analysis of the Spin-Flip equations (1.10) and (1.7) to (1.9), according to [12]. For this analysis, we need to introduce the different following frequencies : ν_x and ν_y respectively x and y modes with respect to zero frequency ($\nu_x+\nu_y = 0$), ν_{inj} is the detuning with respect to zero frequency and finally the detuning ν_i with respect to the x-frequency of the free running VCSEL, as shown in figure 1.6.

$$\nu_x = \frac{\alpha\gamma_a-\gamma_p}{2\pi} \quad \text{and} \quad \nu_y = \frac{\gamma_p-\alpha\gamma_a}{2\pi} \quad \text{and} \quad \nu_i = \nu_{inj}-\nu_x$$

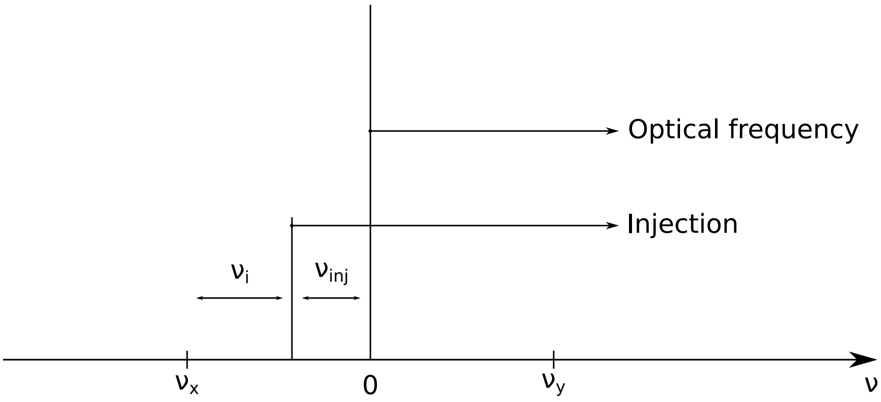

Figure 1.6: Summary of the different detuning and frequencies

While the spin-flip rate is very large compared to the other rates (about 3 orders of magnitude, see [12] [34] and section 2.1 where we give the numerical values of the parameters for our VCSEL), then n is very small, and we can consider $n = 0$.

We write also E_x and E_y as a product of an amplitude function and an exponential taking the phase into account :

$$E_x(t) = A_x(t)\, \exp\left(i(2\pi\nu_{inj}t + \phi_x(t))\right) \tag{1.11}$$
$$E_y(t) = A_y(t)\, \exp\left(i(2\pi\nu_y t + \phi_y(t))\right) \tag{1.12}$$

These expressions for the fields allow us to separate the equations for the amplitudes of the equations for the phases.

All the mathematical calculations are made in appendix A, and we obtain simpler expressions for the model.

$$\dot{A}_x = (\kappa(D-1) - \gamma_a)A_x + \kappa E_{inj} \cos\phi_x \tag{1.13}$$
$$\dot{A}_y = (\kappa(D-1) + \gamma_a)A_y \tag{1.14}$$
$$\dot{\phi}_x = \kappa\alpha(D-1) - 2\pi\nu_i - \alpha\gamma_a - \frac{\kappa E_{inj}}{A_x}\sin\phi_x \tag{1.15}$$
$$\dot{\phi}_y = \alpha(\kappa(D-1) + \gamma_a) \tag{1.16}$$
$$\dot{D} = -\gamma[D(1 + A_x^2 + A_y^2) - \mu] \tag{1.17}$$

From equations (1.13) to (1.17), we study the steady-state solution for $A_x > 0$ and $A_y > 0$ that characterize the solution where both polarizations are excited.

$$\dot{A}_x = \dot{A}_y = \dot{\phi}_x = \dot{\phi}_y = \dot{D} = 0$$

Again, the calculations are given in appendix A, and we obtain :

$$P_{inj} = E_{inj}^2 \tag{1.18}$$
$$P_x = A_{x,0}^2 = \left(\frac{\kappa}{2\gamma_a}\right)^2 \frac{P_{inj}}{1 + \left(\frac{\pi\nu_i}{\gamma_a} + \alpha\right)^2} \tag{1.19}$$
$$P_y = A_{y,0}^2 = \frac{\mu}{1 - \frac{\gamma_a}{\kappa}} - 1 - P_x \tag{1.20}$$
$$\phi_x = -\arctan\left(\frac{\pi\nu_i}{\gamma_a} + \alpha\right) \tag{1.21}$$

We can point out that these relations demonstrate that in the IL+PS solution, the total power $P_x + P_y$ is constant. The experimental study of this phenomenon has been done in [32] and in [12].

These equations describe the states where both x and y polarizations are excited, and will be used for the simulations mapping these states (see section 2.3). We will also see in section 2.2 that we can use the equations of the spin-flip model to analyse the stability of the different states [12] [28].

2 Stability Analysis & Simulations

In this chapter, we study the equations given by the spin-flip model, both theoretically with a linear stability analysis and by simulations. However, to be more accurate in our analysis and simulations, we give the parameters of the VCSEL we will use, according to [12], [31] and [34].

2.1 VCSEL Parameters

2.1.1 Parameters, according to Previous Measurements

In this section, we give the useful parameters of the VCSEL we use in the experiment, so the simulations and the stability analysis can be the most accurate. The different parameters are given in table 2.1, and were extracted for a similar free-running VCSEL [34].

Table 2.1: Parameters of the VCSEL

κ	33 ns^{-1}	γ	2.08 ns^{-1}
γ_a	-0.1 ns^{-1}	γ_s	2100 ns^{-1}
α	2.8	μ	2,29
γ_p	103.34 ns^{-1}	I_{th}	1.602 mA
N_t/N_{th}	0.744	τ_n/τ_e	0.40

In this table, two things need to be pointed out. First the value of μ is a normalization of the bias current corresponding to an injected current of 3.05 mA in the VCSEL. This value is calculated in the program used for the simulations. The expression for μ is given in equation (2.1) according to [34].

$$\mu = \frac{\tau_n}{\tau_e}\frac{\dfrac{I}{I_{th}} - 1}{1 - \dfrac{N_t}{N_{th}}} + 1 \tag{2.1}$$

Where I, I_{th}, N_t, τ_n are the same given in 1.1.3 (respectively current, threshold current, number of carriers at transparency and differential carrier lifetime at the lasing threshold), and N_{th} and τ_e are respectively the number of carriers at threshold and the carrier lifetime at threshold. The relation $\tau_e = e \cdot N_{th}/I_{th}$ gives the link between these variables.

Secondly, the value of the linear dichroism γ_a is supposed here to be constant, but it is not the case, as demonstrated in [34]. We will measure this value for different bias currents for our VCSEL in order to be able to run more accurate simulations. We will expose in this document two different methods that can be used to extract the linear dichroism of the device :

- An usual method, as described in [34].
- A method using the IL+PS region properties.

The value that will be used in the simulation is the one extracted from the second method, that is $\gamma_a = -0.21$ ns^{-1} for $I_{bias} = 3.0$ mA.

2.1.2 Measurement of the Linear Dichroism

In this section, we discuss the value of the linear dichroism γ_a as a function of the bias current, using the procedure of [34] to measure it.

Experimental Setup

The experimental setup we use in order to measure the linear dichroism is really simple. We directly connect the VCSEL to a high-resolution optical spectrum analyser (BOSA), that we describe precisely in section 3.1.2.

Measurements & Results

The measurement of the linear dichroism, as explained in [34], is the following. We measure for various currents the width of the non-lasing mode of the VCSEL (using averaging options on the BOSA) in order to get an intermediate parameter γ_0, the effective dichroism given by (2.2). In this equation, the width of the lasing mode is insignificant and cannot be measured with the BOSA.

$$\gamma_0 = \pi\left(\Delta\nu_{Lasing} - \Delta\nu_{nonLasing}\right) \simeq -\pi \cdot \Delta\nu_{nonLasing} \tag{2.2}$$

The absolute value of γ_0 has a minimum value at an injected current of 6.7 mA (corresponding to the current at which a polarization switching is observed). This minimum is the non-linear dichroism γ_{non}. Finally, γ_a is given by (2.3). We give in figure 2.1 and in table 2.2 the results of the measurements.

$$\gamma_a = \operatorname{sgn}(\gamma_0) \cdot \left[\frac{|\gamma_0| - \gamma_{non}}{2}\right] \tag{2.3}$$

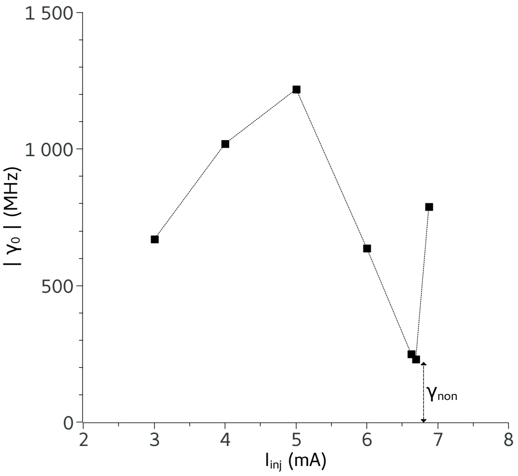

Figure 2.1: Absolute value of the effective dichroism as a function of the current. The value of the non-linear dichroism is also indicated

Note :

$$\operatorname{sgn}(x) = \frac{|x|}{x} \quad \text{for } x \neq 0$$

Table 2.2: Values of the linear dichroism and the effective dichroism for various values of the injected power

I_{inj} (mA)	γ_0 (GHz)	γ_a (GHz)
3.0	-0.67	-0.22
4.0	-1.02	-0.40
5.0	-1.22	-0.50
6.0	-0.637	-0.20
6.63	-0.25	-0.01
6.69	-0.23	0
6.88	0.79	0.28

Note : We will present another way to measure γ_a in section 3.2.2. However, results given by the two methods do not perfectly agree. Further work must be done in order to understand this point [34] [35] [36] [37].

2.2 Stability Analysis

In this section, we focus on the stability of the steady-state obtained in section 1.3.3, state in which both polarizations are excited ($A_x > 0$ and $A_y > 0$). This stability analysis uses the work [28], which model is the same as the one we have when a suitable variable change is made. This variable change, and the mathematical steps of the stability analysis, are given in appendix B.

The model used in [28] is the following, with TE optical injection (same conditions), and we demonstrate in appendix B the variable change from our model to this one.

$$\frac{\mathrm{d}E_1}{\mathrm{d}t} = (1+i\alpha)NE_1 + \gamma\exp(i\Delta t) \tag{2.4}$$

$$\frac{\mathrm{d}E_2}{\mathrm{d}t} = k(1+i\alpha)(N-\beta)E_2 \tag{2.5}$$

$$T\frac{\mathrm{d}N}{\mathrm{d}t} = P - N - (1+2N)(|E_1|^2 + |E_2|^2) \tag{2.6}$$

The change of variable is given in appendix B, and the new parameters are identified as functions of the spin-flip model parameters :

$$\gamma = \frac{E_{inj}}{2\sqrt{2}\left(1+\frac{\gamma_a}{\kappa}\right)} \tag{2.7}$$

$$\Delta = \frac{\pi\nu_i}{\kappa\left(1+\frac{\gamma_a}{\kappa}\right)} \tag{2.8}$$

$$k = 1 \tag{2.9}$$

$$\beta = -\frac{\gamma_a}{\kappa+\gamma_a} \tag{2.10}$$

$$T = \frac{2\kappa\left(1+\frac{\gamma_a}{\kappa}\right)}{\gamma} \tag{2.11}$$

$$P = \frac{\mu - \left(1+\frac{\gamma_a}{\kappa}\right)}{2\left(1+\frac{\gamma_a}{\kappa}\right)} \tag{2.12}$$

From these equations, it is possible to write, by doing the same kind of transformations (equations (2.13) and (2.14)) as those done to the flip-spin model (section 1.3.3 and appendix A), the following system. The equation for ϕ_2 is not given for it passively depends on N.

$$E_1 = R_1\exp(i\Delta t + i\phi_1) \tag{2.13}$$

$$E_2 = R_1\exp(i\phi_2) \tag{2.14}$$

$$\dot{R}_1 = NR_1 + \gamma\cos\phi_1 \tag{2.15}$$

$$\dot{\phi}_1 = -\Delta + \alpha N - \frac{\gamma}{R_1}\sin\phi_1 \tag{2.16}$$

$$\dot{R}_2 = k(N-\beta)R_2 \tag{2.17}$$

$$T\dot{N} = P - N - (1+2N)(R_1^2 + R_2^2) \tag{2.18}$$

We now study the steady state for these equations. We study in particular the stability of the state where both polarizations are excited, a state we call *Injection locking + Polarization Switching (IL+PS)*. This state is verified for $R_1 > 0$ and $R_2 > 0$. Once again, the mathematical steps will be given in appendix B, and we give here the result of the analysis, according to [28].

In appendix B, we study the steady-state of IL+PS, and then the stability by studying small perturbations around the steady-state (we note for a variable $V : V_0 + \delta V$ where δV is small. $\delta V_1 \cdot \delta V_2$ become insignificant). We obtain the following matrix system :

$$\dot{X} = A \cdot X \tag{2.19}$$

Where :

$$X = \begin{pmatrix} \delta R_1 \\ \delta \phi_1 \\ \delta R_2 \\ \delta N \end{pmatrix} \text{ and } A = \begin{pmatrix} \beta & R_{1,0}(\Delta - \alpha\beta) & 0 & R_{1,0} \\ \dfrac{-(\Delta - \alpha\beta)}{R_{1,0}} & \beta & 0 & \alpha \\ 0 & 0 & 0 & kR_{2,0} \\ \dfrac{-2(1+2\beta)}{T} R_{1,0} & 0 & \dfrac{-2(1+2\beta)}{T} R_{2,0} & \dfrac{-(1+2P)}{T(1+2\beta)} \end{pmatrix}$$

The characteristic polynomial of A is given accordingly to [28] and our calculations in appendix B :

$$\lambda^4 + a_1\lambda^3 + a_2\lambda^2 + a_3\lambda + a_4 = 0 \tag{2.20}$$

Where :

$$a_1 = \frac{1+2P}{T(1+2\beta)} - 2\beta \tag{2.21}$$

$$a_2 = \frac{-2\beta}{T}\frac{(1+2P)}{(1+2\beta)} + (\Delta - \alpha\beta)^2 + \beta^2 + \frac{2(1+2\beta)}{T}(R_{1,0}^2 + kR_{2,0}^2) \tag{2.22}$$

$$a_3 = \frac{1}{T}\left[\frac{(1+2P)}{(1+2\beta)}((\Delta - \alpha\beta)^2 + \beta^2) + 2(1+2\beta)\left[(\alpha(\Delta - \alpha\beta) - \beta)R_{1,0}^2 - 2k\beta R_{2,0}^2\right]\right] \tag{2.23}$$

$$a_4 = \frac{2kR_{2,0}^2}{T}(1+2\beta)((\Delta - \alpha\beta)^2 + \beta^2) \tag{2.24}$$

According to [28], the conditions for the stability of the steady state are given by the Routh-Hurwitz conditions :

$$a_1 > 0, \quad a_3 > 0, \quad a_4 > 0, \quad a_1a_2a_3 - a_3^2 - a_1^2a_4 > 0 \tag{2.25}$$

With the equations (2.21) to (2.24) for the parameters of the Routh-Hurwitz conditions, the equations (2.7) to (2.12) giving the correspondence between the two models and the table 2.1 giving the parameters of our VCSEL, we can get a graphical visualisation of the regions where both injection locking and polarization switching states are stable, as a function of the injected power and the detuning. These regions are given for different currents in figure 2.2(a) to 2.2(c).

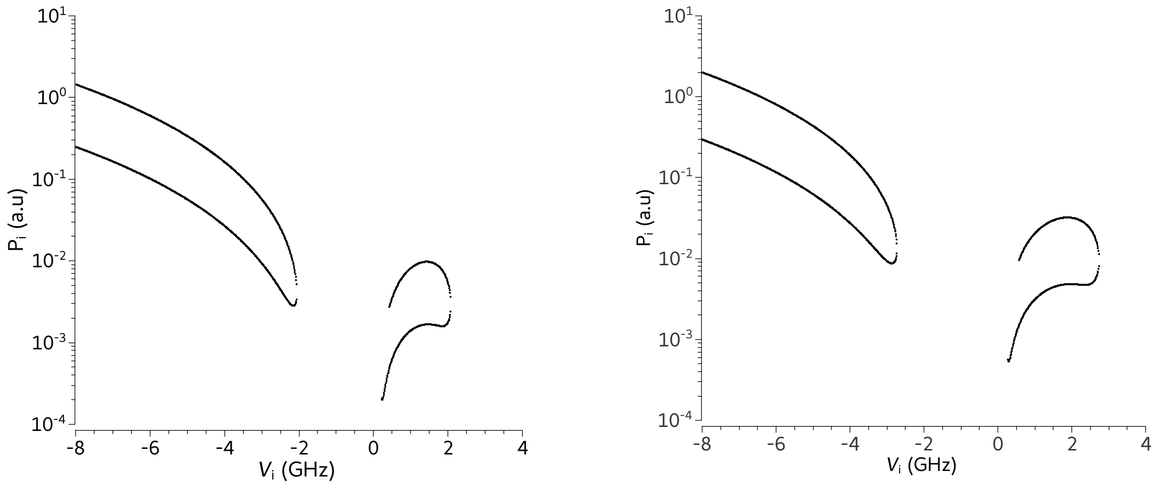

(a) I=3.00 mA (b) I=4.00mA

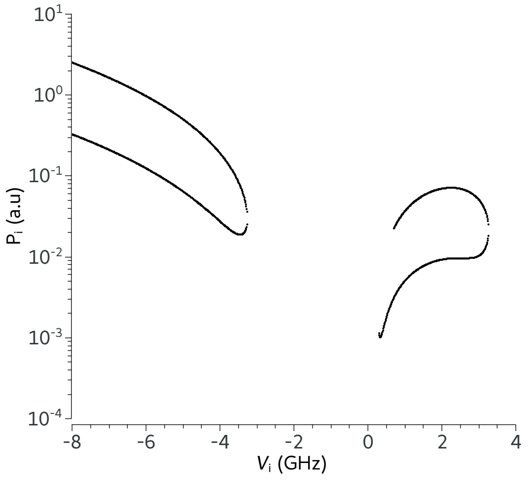

(c) I=5.00mA

Figure 2.2: Theoretical values of injected power for which IL+PS is stable as a function of ν_i, for various values of I. These maps are found according to the stability analysis [28]

In these maps, we clearly see two regions, that are closed, where both injection locking and polarization switching (IL+PS) are stable. The shapes of these regions are really similar for the different bias currents, except for the maximum detuning value of the negative area (respectively -2, -2.6 and -3 GHz), and the width of the regions. Although is the width of the regions increasing with the injected current, the lower boundary of the region are similar for each current, even if there are small differences. The values of the linear dichroism for each bias current are respectively -0.21, -0.26 and -0.30 ns^{-1}.

These theoretical results will be compared to the simulations given by the steady-state of the Spin-Flip model (section 2.3), and the experimental measurements (3.2.1).

The stability analysis done in [28] do not only focus on this IL+PS state, but also gives the boundaries of the region where the IL state is stable for the VCSEL subject to parallel optical injection. We did this study in order to compare the results with the experimental maps we will give in section 3.3 The theoretical results are given in a following paragraph about bistability.

2.3 Simulations

In this section, we use the equations (1.10) and (1.7) to (1.9) given by the Spin-Flip Model to run numerical computations in order to obtain numerically the regions where injection-locking and polarization-switching are stable. Spontaneous emission noise terms have been included in the model, as explained in [34]. To do this, we simulate the variation of the injected power from a minimal value to a maximum value. And then from the maximum value to the minimum value in order to simulate the bistability of the system.

More specifically, the spin-flip model is numerically integrated with an integration time 0.01 ps, a sampling time 5 ps and the swipe in injected power is done in 75 time windows of 327.68 ns, after a 80 ns transient.

The shape of the injected power as a function of the time is exponential, so that the logarithm of the injected power as a function of the time is linear (see figure 2.3). We can also choose the time we stay on each step of injected power in order to be as close as possible of the steady-state.

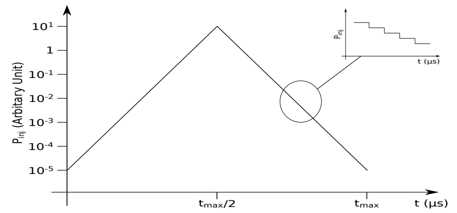

Figure 2.3: Shape of the injected power as a function of time.

2.3.1 IL+PS state & Bistability

We first study the region of injected power where injection-locking and polarization-switching occur simultaneously (IL+PS) as a function of the detuning. As explained before, we use the spin-flip model to run numerical computations, and we obtain the figure 2.4 for an injected current of 3.05 mA. We define a threshold in order to detect where IL+PS is stable : the power of the y-polarization mode is greater than 0.5. And we work with a $t_{max} = 48.65$ μs. The shape is pretty similar to the one given by the theoretical approach. We will see a better comparison in part 2.3.3.

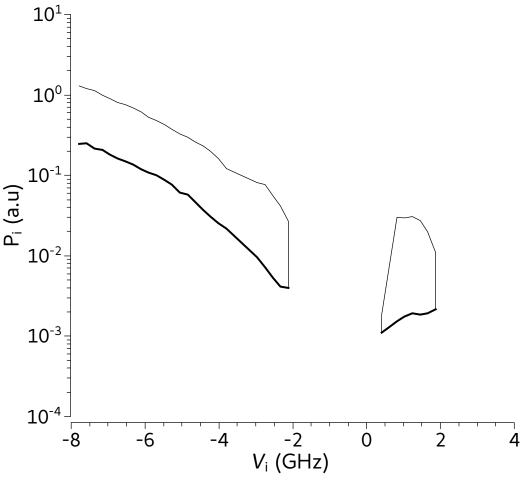

Figure 2.4: Region of injected power P_i where IL+PS state is stable as a function of the detuning ν_i, for I= 3.05 mA. We explore bistability in the following section

We focus on this section on the bistability of the two boundaries of the IL+PS state, still using the spin-flip model. We now increase and then decrease the injected power as a function of time, as shown in figure 2.3, and record the boundary of the state IL+PS. We obtain the figures 2.5(a) to 2.5(c) for different injected currents.

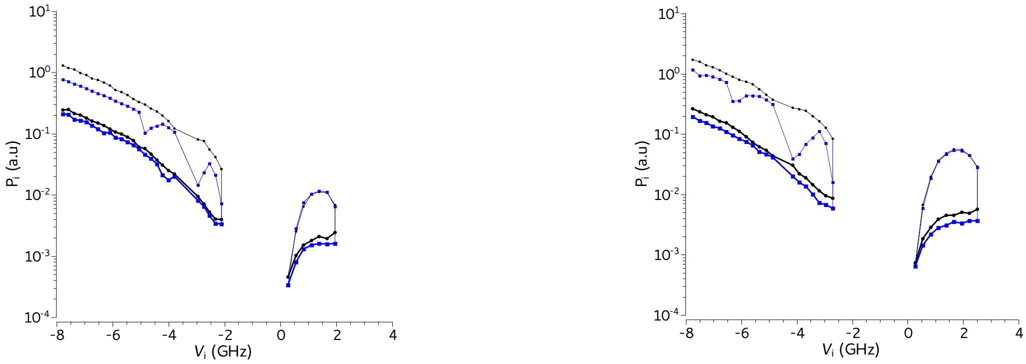

(a) I=3.00 mA

(b) I=4.00mA

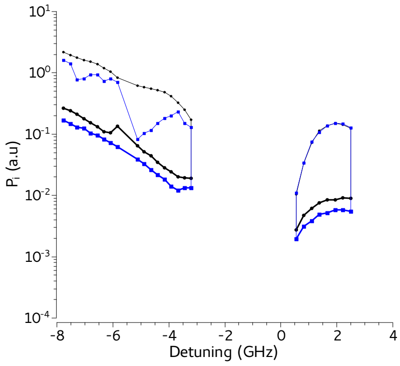

(c) I=5.00mA

Figure 2.5: Simulated values of injected power for which IL+PS is stable as a function of ν_i, for different values of injected current I. The blue lines in (a), (b) and (c) marks the lower boundaries of the bistable region.

As we can see in these three maps, the global shape of the region where IL+PS is stable is similar for the different currents. We can point out three main differences :

- The region shift upwards when increasing the injected current
- The maximum ν_i value of the area appearing at negative detuning decrease when increasing the injected current
- The size of the bistability does not change much, but still increase when increasing the injected current.

Another way of showing the bistability between the IL+PS state and the state above the boundary, which is injection locking of the parallel polarization mode on the injected light of the master laser, is to give (in figure 2.6) the optical spectra obtained by numerical integration of the spin-flip model. These two spectra are obtained for the same injection parameters (bias current, frequency detuning and injected power) but figure 2.6(a) is obtained after an increase of $\mathrm{P_i}$ and figure 2.6(b) is obtained after a decrease of $\mathrm{P_i}$. More specifically, the integration time, the sampling time and the length of the temporal windows are the same as previously, and the spectra are obtained with an average over 20 temporal windows, after a 10 windows continuous sweep in $\mathrm{P_i}$.

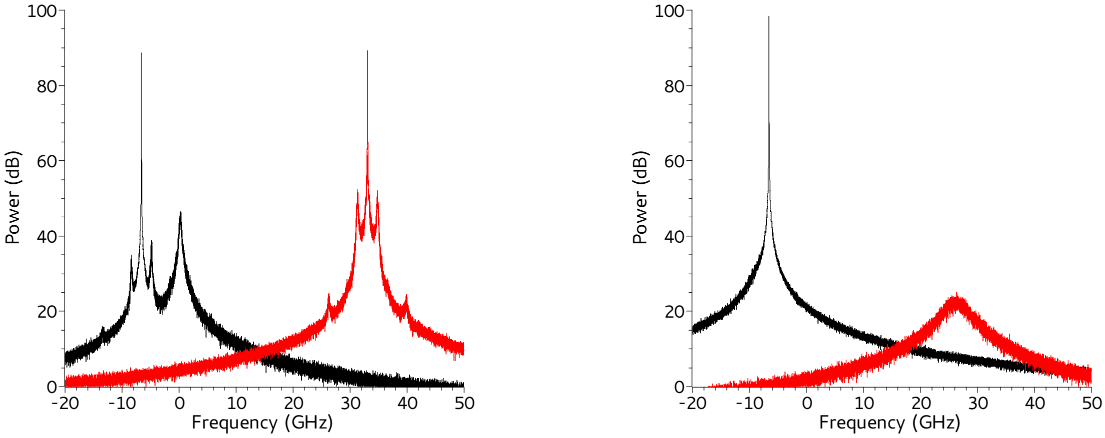

(a) IL+PS state (increasing $\mathrm{P_i}$) (b) IL state (decreasing $\mathrm{P_i}$)

Figure 2.6: Theoretical optical spectra obtained for injection parameters I $=$ 3.00 mA, $\nu_i = -6.6$ GHz and $\mathrm{P_i} = 0.74$ (a.u) when (a) increasing $\mathrm{P_i}$ and (b) decreasing the level of injection.

These spectra are obtained for a realistic value of the spontaneous emission noise previously obtained $\beta_{SF} = 6.5\ 10^{-4}$ [34]. This spontaneous emission noise results in the excitation of some satellite peaks in the IL+PS optical spectra, in particular, the parallel mode of the free-running slave VCSEL, satellite peaks with a frequency difference with regard to the main peaks at the relaxation oscillation frequency $=$ 2.08 GHz for this bias current(2.26), and peaks with a frequency difference with the main peaks at the frequency detuning ν_i.

$$\nu_r = \frac{\sqrt{2\kappa\gamma\,(\mu-1)}}{2\pi} \tag{2.26}$$

2.3.2 Reproducibility

A very important issue of simulations is the reproducibility of the results. Considering the noise in the simulation, it is important to be sure that several simulations will have the same result. In this aim, we run the simulation several times in order to characterize the reproducibility. In this study, we focus only on one value of the detuning, randomly selected : $\nu_\mathrm{i} = -7$ GHz, and we give in table 2.3 the mean value, the standard deviation and the variance for the value of the injected power of the boundaries of the IL+PS region for 10 consecutive simulations, both when increasing or decreasing the injected power. These values confirm that the reproducibility of the simulation is very good. We can expect the same kind of reproducibility for other values of the detuning.

Table 2.3: Mean value, standard deviation and error rate (%) for 10 simulations. LB is Lower Boundary, UB is Upper Boundary

	Mean value	Standard Deviation (SD)	SD/Mean (%)
LB, Increasing P_{inj}	0.08827	0.00344	3.90 %
UB, Increasing P_{inj}	0.91452	0.01256	1.36 %
UB, Decreasing P_{inj}	0.57424	$9.61342 \cdot 10^{-4}$	0.167 %
LB, Increasing P_{inj}	0.06981	$3.21387 \cdot 10^{-3}$	4.60 %

2.3.3 Comparison with the Theory given by the Stability Analysis

In this section, we give a comparison between the result obtained by the theoretical point of view (linear stability analysis of the IL+PS steady state) and the result given by the simulation of steady-state of the spin-flip model. The comparison is given by figure 2.7.

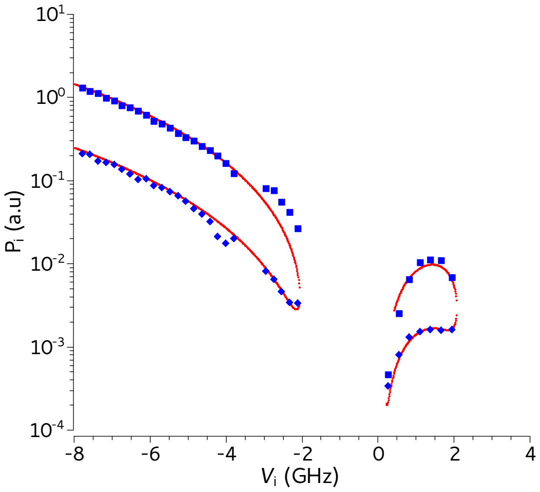

Figure 2.7: Comparison between theoretical (black) and simulated (blue) values of injected power for which IL+PS is stable as a function of ν_{i}, for $I = 3.05$ mA.

We see that the shapes are extremely similar, as well as the extrema of the detuning for the region. Some mismatch can be observed in the positive frequency detuning region, and a lack of values given by the simulation around -3.5 GHz. This last mismatch is a result of the choice of the threshold value in the simulation software. This figure confirm that we reach the steady-state in our simulations. However, for smaller values of t_{max} ($t_{max} < 10^3$ ns), the simulated and theoretical regions are shifted from one another. This can be explained by the theory of delayed bifurcation [38] we will see more precisely in appendix C.

In order to quantify the delay of the bifurcation from P1 state (periodic behaviour) to IL+PS state and from IL+PS state to IL state (Injection locking), we simulate the delay for one particular value of detuning ($\nu_i = -7$ GHz), and different values of t_{max}. Then we plot on figures 2.8(a) and 2.8(b) the difference between the injected power of the transition given by the simulation and the injected power of the transition given by the theory (linear stability analysis).These figures show the delay of the system with regard to the steady-state for the two boundaries.

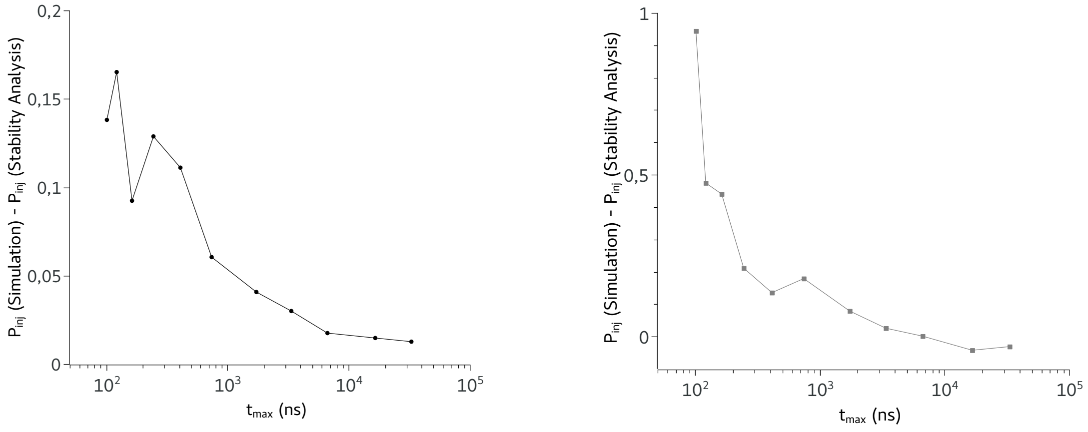

(a) Lower boundary (b) Upper boundary

Figure 2.8: Difference between simulated and theoretical values of the upper and lower boundary of the IL+PS state as a function of t_{max} for a detuning $\nu_i = -7$ GHz and an injected current $I = 3.05$ mA

We could try to find a model in order to give the value of t_{max} for which the steady-state is reached. And we must point out that the value of the injected power for the boundaries is function of the value we choose for the threshold of the y-polarization.

We also give in figure 2.9 the map given by the linear stability analysis performed for the IL+PS steady-state, and for the IL steady-state, as performed for the TE steady-state in [28], for a bias current $I = 3.00$ mA. In this figure, the IL steady-state present two boundaries : SN_1 corresponding to a saddle-node bifurcation, and H_1 corresponding to a Hopf bifurcation. We see in this figure that there is a region where the system is both in the IL+PS region and in the IL region. This induce the bistability, and a comparison with the experimental results gives very good agreement.

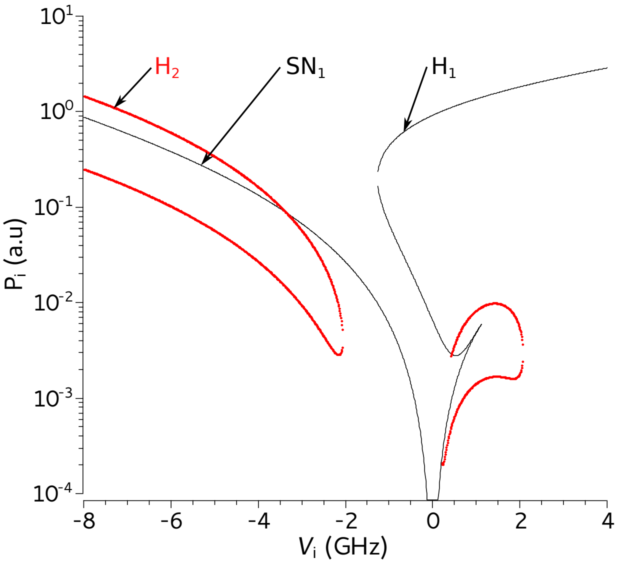

Figure 2.9: Theoretical map giving the values of injected power for which IL+PS is stable as a function of ν_{i} (in red), and the values of injected power for which the IL state is stable (in black) for $I = 3.00$ mA.

3 Experimental Setup & Results

In this chapter, we present the experimental setup for parallel optical injection that we use in this work, and we give the characteristics of the experimental equipment. In a second section, we present the different measurements we made, in particular maps of stability of the IL+PS state, and complete maps of the polarization dynamics of the VCSEL.

3.1 Experimental Setup

First we give the characteristics of the all-fiber experimental setup we use in our measurements of the polarization dynamics of VCSELs subject to optical parallel injection. All the measurements are done on a similar VCSEL to the one we gave the characteristics in table 2.1 well described in [34], at a temperature of $T = 298.00 \pm 0.05$ K.

3.1.1 Experimental Setup

The all-fiber experimental setup (figure 3.1) is the following. The parallel optical injection is performed by the injection of the light of the master laser - a tunable laser (TL) - into a commercial 1550-nm VCSEL (RayCan) using a three-port optical circulator. The VCSEL single transverse mode regime is the linear polarization we call "parallel" polarization. The parallel polarization of the injected light is controlled by the first polarization controller (PC1), and a second polarization controller (PC2) is used to measure the polarization of the setup. We are able to control the value of the injected power in the VCSEL via a variable attenuator (VA) and measure the injected power after the optical coupler with a power meter (PM).

The second polarization controller (PC2) is connected to a polarization beam splitter (PBS) to select select parallel and orthogonal polarizations, analysed by the power meters (PM1 and PM2) or by the BOSA (high-resolution optical spectrum analyser). We give more precisions about the experimental equipment in the following section 3.1.2.

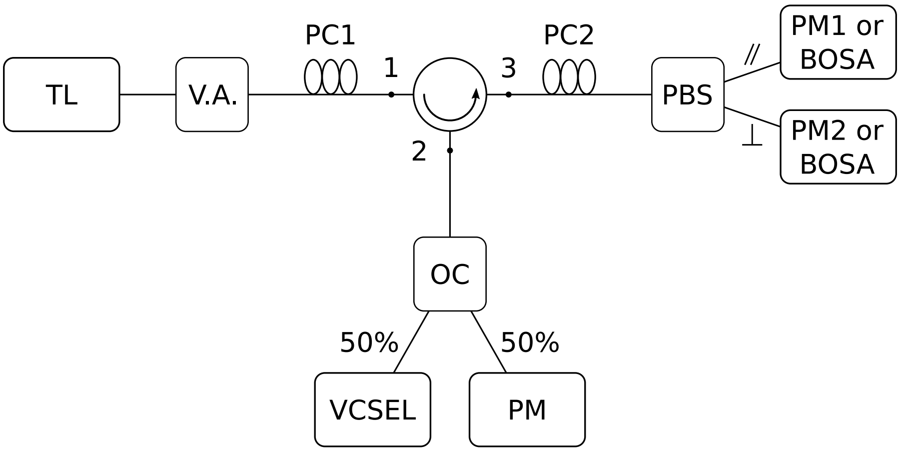

Figure 3.1: Experimental Setup for parallel optical injection in the VCSEL. Tunable laser (TL), variable attenuator (VA), polarization controllers (PC1 and PC2), optical coupler (OC), power meter (PM, PM1 and PM2), polarization beam splitter (PBS), high-resolution optical spectrum analyser (BOSA)

3.1.2 Experimental Equipment

We give in this section a description and the characteristics of the experimental equipment. We can find the description in the documentation of the equipment, and in this work we only give important characteristics based on [32].

Tunable laser (TL)

We use for our experiment the semiconductor tunable laser *Anritsu Tunics Plus.* Its wavelength range is 1500 to 1625 nm with a resolution of 1 pm and a maximum output power of 8 mW.

High-resolution Optical Spectrum Analyser (BOSA)

We use for optical spectra analysis the *Aragon Photonics BOSA 210*, that uses stimulated Brillouin scattering spectroscopy. The BOSA's maximum resolution is 10 MHz at an 80 dB dynamical range and measurements are nearly instantaneous. However, the BOSA operating require a tunable laser in order to achieve high resolution analysis, and this tunable laser heats when measuring, leading to shifts of spectra. And thereby we cannot fully trust the absolute wavelength given by the BOSA, but the problem can be avoided by pausing and running again the BOSA.

Power Meter (PM)

In the experimental setup, we use several optical-fiber power meters (*Thorlabs PM20*) in order to record output powers. The sensor is a InGaAs diode and the covered wavelength range is 400 to 1700 nm. The measurements can be done in W or in dBm. The measurement range in dBm is from -60 to 20 dBm with an uncertainty of ±0.25 dB. In our experiment we measure in W, typically from 10^{-6} to 10^{3} μW.

Variable Attenuator (VA)

The variable attenuator we use in our experimental setup is the *OZ Optics Digital Variable Attenuator DA-100.* The attenuation in dB can be chosen through a keypad by the user in a range from -0.1 to -60 dB. The attenuator is simply a mechanical blocking of the light.

Optical Coupler (OC)

The experimental 50/50 optical coupler is the *Newport F-CPL-F12155.* The center wavelength of use of the device is 1550 nm, its return loss is 55 dB and its maximum insertion loss is 3.4 dB.

Polarization Controller (PC)

Two polarization controllers are used in the experimental setup. We use the *Fiber U-Bench polarization controller Thorlabs FBR05* that consists of one $\lambda/2$ and two $\lambda/4$ waveplates we can rotate in order to select the desired polarization at the end of the optical fiber.

Fiber Optical Circulator

We use a non-polarisation maintaining *Newport* fiber optical three-ports circulator. its wavelength center of use is 1550 nm. The circulator operating is the following. Light entering through port one exits through port 2 and entering through port 2 exits through port 3 without reciprocal.

Polarization Beam Splitter (PBS)

We use the *Newport F-PBC-15-SM-FA* as a polarization beam splitter. The device split the signal from one optical fiber into its two polarization components (parallel and orthogonal). The center wavelength of use of the device is 1550 nm, and the ratio of parallel to orthogonal loss is 2.25 dB.

Fiber Connectors

In our all-fiber experimental setup, we use two kind of connectors that cannot be directly connected from one another : the Physical Contact (PC) connector and the Angled Physical Contact (APC) connector that have a 8° angle for the contact (see figure 3.2).

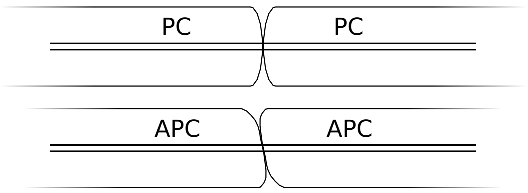

Figure 3.2: Connection scheme for APC and PC fiber connectors

3.2 Measurements & Results

We give in this section the measurements and the result of the analysis of dynamics of the polarization of the VCSEL. In a first section, we focus only on the IL+PS state (injection-locking and polarization switching), and then we describe the complete study of dynamics of the VCSEL subject to parallel optical injection.

When describing the complete dynamics of the polarization of the VCSEL, we will give complete maps of dynamics, and for each region of the map, characteristic spectrum obtained using the BOSA and time traces obtained using an oscilloscope with a 12 GHz bandwidth.

3.2.1 Stability of the IL+PS Region & Bistability

In this section, we characterize the regions where both injection locking and polarization switching (IL+PS) are stable. In order to do it, we use the tunable laser as a master laser to fix a detuning of injection with regard to the free running VCSEL, and for each value of the detuning, we increase and then decrease the injected power of the master laser thanks to the variable attenuator. The variable attenuator allow us to create a step of attenuation. Most of the measurements are done using a step of 0.1 dB on the attenuator.

We analyse the VCSEL output light with the BOSA, and we are able to clearly distinguish the IL+PS state from other states. We give in figure 3.3(a) an example of IL+PS spectrum given by the BOSA, and in figures 3.4(a) to 3.4(c) the maps giving regions where IL+PS is stable for various values of the injected current. In order to show the bistability properties of the IL+PS state, we also give in figure 3.3(b) the experimental optical spectra obtained for the same injection parameters as in figure 3.3(a), but when decreasing the injected power.

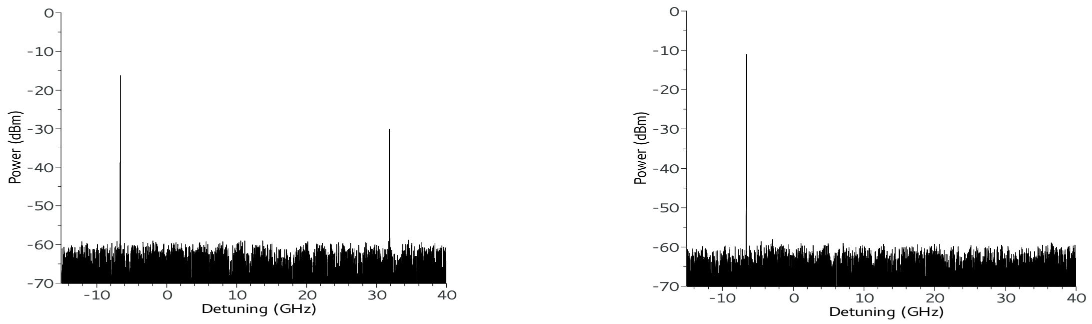

(a) IL+PS state (increasing $\mathrm{P_i}$) (b) IL state (decreasing $\mathrm{P_i}$)

Figure 3.3: Experimental optical spectra obtained for injection parameters I = 3.00 mA, $\nu_i = -6.6$ GHz and $\mathrm{P_i} = 421\ \mu$W when (a) increasing $\mathrm{P_i}$ and (b) decreasing $\mathrm{P_i}$.

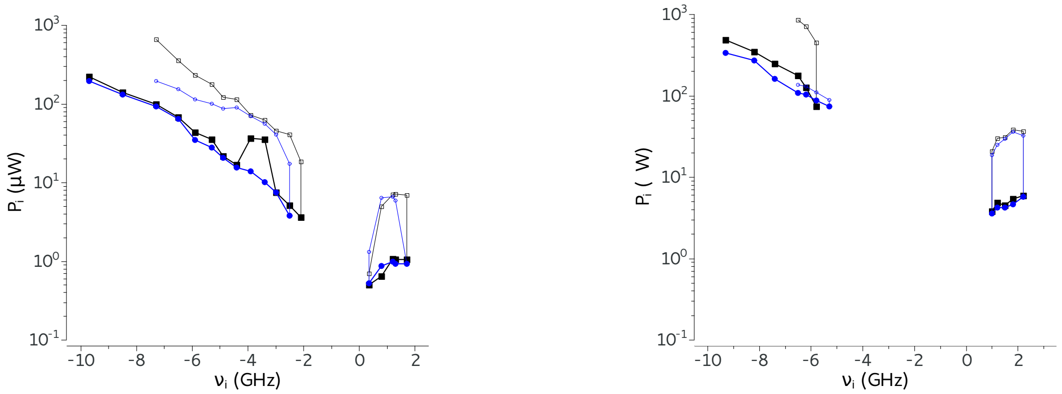

(a) I=3.00 mA (b) I=4.00 mA

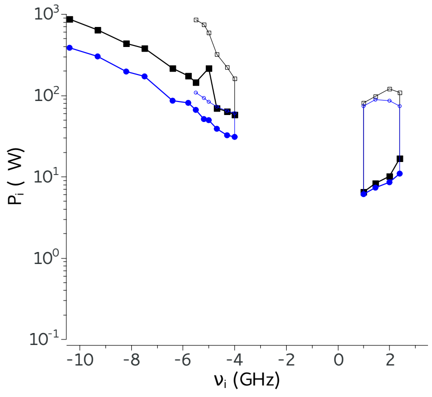

(c) I=5.00 mA

Figure 3.4: Measurements of the regions where IL+PS is stable for different values of I. Black is when increasing the injected power, and blue is when decreasing P_{inj}

In the previous figures, regions with black boundaries are obtained when increasing the injected power, and regions with blue boundaries are obtained when decreasing $\mathrm{P_{inj}}$.

The regions for an injected current of 3 mA are very similar than the one given by the linear stability analysis and the simulation of the Spin-Flip model. Both the shape and the extrema values for the detuning are similar. However, we observe when increasing the injected power that the lower boundary of the region shift in regard with the simulation (for $-5 < \nu_i < -3$ GHz). We observe here another behaviour : a period doubling in the parallel polarization.

The map for an injected current of 5 mA is rather similar than the ones obtained by simulation and stability analysis with regard to the shape and the extrema values of the detuning. For an injected current of 5 mA, the boundary are generally at higher values of injected power than for $I = 3$ mA, and the size of the regions is increased.

The map for an injected current of 4 mA is a bit different. The region within the positive values of detuning is very similar to the one obtained in the simulations. However, in the negative detuning region, the extrema value of ν_i where IL+PS can be observed is rather different than the one obtained in the simulations. A way to explain that is the fact that another behaviour is stable for this region of the frequency detuning-injected power plane.

Moreover, for each value of injected current, we are able to observe a really large number of behaviour for the dynamics of the VCSEL subject to parallel optical injection. Some behaviours have been observed, and some new behaviours have been observed with this experiment. In order to characterize these new behaviours in the polarization dynamics of the VCSEL, we will in section 3.3 record every behaviour and plot maps of dynamics.

3.2.2 Extraction of the linear dichroism

We can notice that for a large region (negative values of the detuning) the experimental and theoretical ratios between the upper and the lower boundaries are almost constant, and theoretically depending in the linear dichroism.

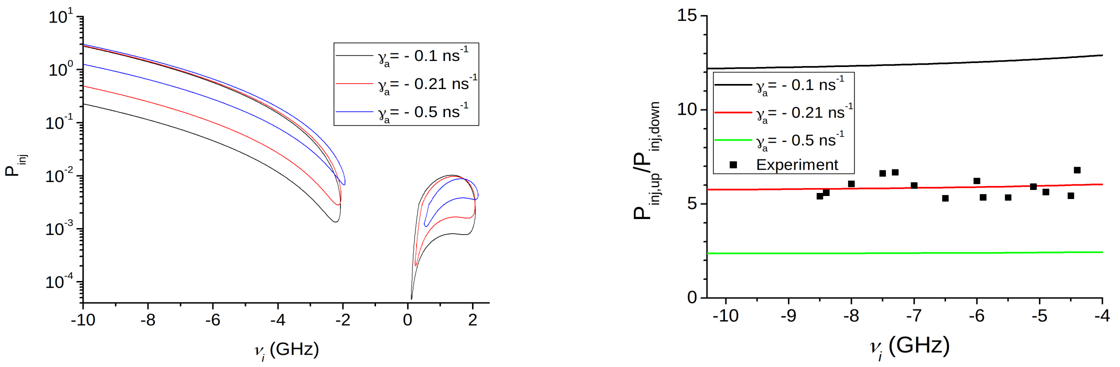

(a) IL+PS stability for various γ_a

(b) $P_{inj,up}/P_{inj,down}$ for various γ_a

Figure 3.5: Extraction of the linear dichroism using the width of the region where IL+PS is stable. (a) give the theoretical map for various values of γ_a and (b) the ratio $P_{inj,up}/P_{inj,down}$ experimentally and theoretically for various values of γ_a

In figures 3.5(a) and 3.5(b) are respectively given the theoretically obtained regions where IL+PS is stable for various values of the linear dichroism, and a comparison between experimental and theoretical ratio $P_{inj,up}/P_{inj,down}$ for various γ_a. For large and negative values of the detuning $(-10 < \nu_i < -5)$, this ratio is almost constant (change of 3%) and the dependency on γ_a is strong.

The ratio can be mathematically approximate through the Routh-Hurwitz condition $a_1 a_2 a_3 - a_3^2 - a_1^2 a_4 = 0$ and is given by (3.1) :

$$\frac{P_{inj,up}}{P_{inj,down}} \simeq \frac{\gamma\mu}{4|\gamma_a|} \tag{3.1}$$

Finally, figure 3.5(b) shows the very good agreement between experimental and theoretical results for $\gamma_a = -0.21$. The value measured in section 2.1.2 with another method is $\gamma_a = -0.22$. In conclusion, this new and simple way of measuring this parameter give good results.

3.2.3 Bistability - Comparison Theoretical and Experimental Maps

Finally in this section, we give the comparison between the experimental stability maps of the IL+PS region in the injected power-frequency detuning plane, and the stability maps obtained from the linear stability analysis. More precisely, we plot on the one hand the region given by the linear stability analysis of the IL+PS steady-state and the boundaries of region where the IL state is stable, both given by [28], and on the second hand the experimental values for the IL+PS boundaries and the IL transition. We separate the experimental values obtained when increasing the injected power (figure 3.6(a)), and the experimental values obtained when decreasing the injected power (figure 3.6(b)). the conversion factor from the experimental to the theoretical values is 1 (a.u) ↔ 565.76 μW.

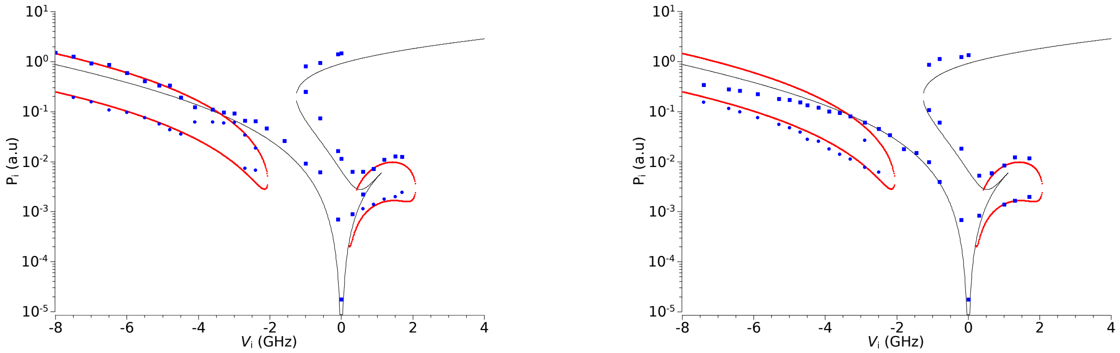

(a) Increasing $\mathrm{P_i}$ (b) Decreasing $\mathrm{P_i}$

Figure 3.6: Comparison Theory and Experimental IL+PS - IL maps & Bistability. In red is given the regions where IL+PS is stable, in black the boundaries of the IL state according to [28], and in blue the experimental values for the same boundaries, for (a) an increase of $\mathrm{P_i}$, and (b) a decrease of $\mathrm{P_i}$

In these figures, we see that the experimental values for the IL transition are in good qualitative agreement with the theoretical values, as well as the IL+PS region, in particular with regard to the bistability region when comparing the two maps.

In order to show how the theoretical linear stability analysis explain the experimental bistability between the IL+PS state and the IL state, we focus on the upper boundary of the IL+PS region, corresponding to the SN_1 boundary of the IL region for $\nu_i < -3$ GHz. We see in figure 3.6(a), corresponding to the experimental values when increasing the injection level, that this boundary matches perfectly the IL+PS boundary given by the linear stability analysis. However, when focussing on figure 3.6(b), that is when decreasing $\mathrm{P_i}$, the boundary follows qualitatively the IL state boundary given by the linear stability analysis of the IL steady state.

The mismatches between experimental and theoretical values can be explained by the parameters of the VCSEL we give in table 2.1 and we have used to get the theoretical values. Indeed, these parameters have been extracted for a similar free-running VCSEL, and not exactly the VCSEL used in the experiment. Secondly, the stability maps for other values of the bias current do not give consistent result with regard to the experimental results. This can be explained by the large variety of non-linear dynamics that can be observed for this VCSEL subject to parallel optical injection. These dynamics will be described in the following section, as well as a complete mapping of the non-linear dynamics of the VCSEL for various bias currents.

3.3 Complete Maps of the VCSEL Dynamics

3.3.1 Maps of the VCSEL Dynamics

In this section, we report an experimental description of the complete dynamics of a VCSEL subject to parallel optical injection. We give the maps of dynamics for various values of the injected current ($I = 3$ mA and $I = 5$ mA). And for each value of the injected current, we give the map obtained when increasing the injected power (resp. figures 3.7(a) and 3.8(a)), and the map obtained when decreasing the injected power (resp. figures 3.7(b) and 3.8(b)). We see that new regions appears for the first time.

Indeed, we observe behaviours that have been well studied [12] [21] [20] : periodic behaviour in parallel polarization like limit cycle (P1) period doubling (P2) and period quadrupling (P4), stable injection locking (IL), chaotic behaviour (CH) and injection locking + polarization switching (IL+PS). We also record new behaviours : periodic behaviour in both polarization (P1 both), period doubling in both polarizations (P2 both), chaotic behaviour in both polarization (CH both).

And finally two behaviours that result from a switching in time between two stable states : (P2+P1 both) resulting from a switching between a period doubling in the parallel polarization (P2) and a limit cycle appearing simultaneously in both polarizations (P1 both); and (P1+PS) resulting from the switching in time between a limit cycle in the parallel polarization (P1) and the IL+PS state. These new regions are reported on the following maps, and the spectra and time traces are given below in order to characterize the properties of each behaviour, and in particular the very new ones. The maps report very consistent result with regards to previous work of theoretical and experimental mapping of non-linear dynamics of semiconductors and VCSELs [21] [20] [39] [23], in particular regarding the shapes of the regions. However, we report in these maps new states, mostly states with non-linear dynamics appearing simultaneously in both polarizations.

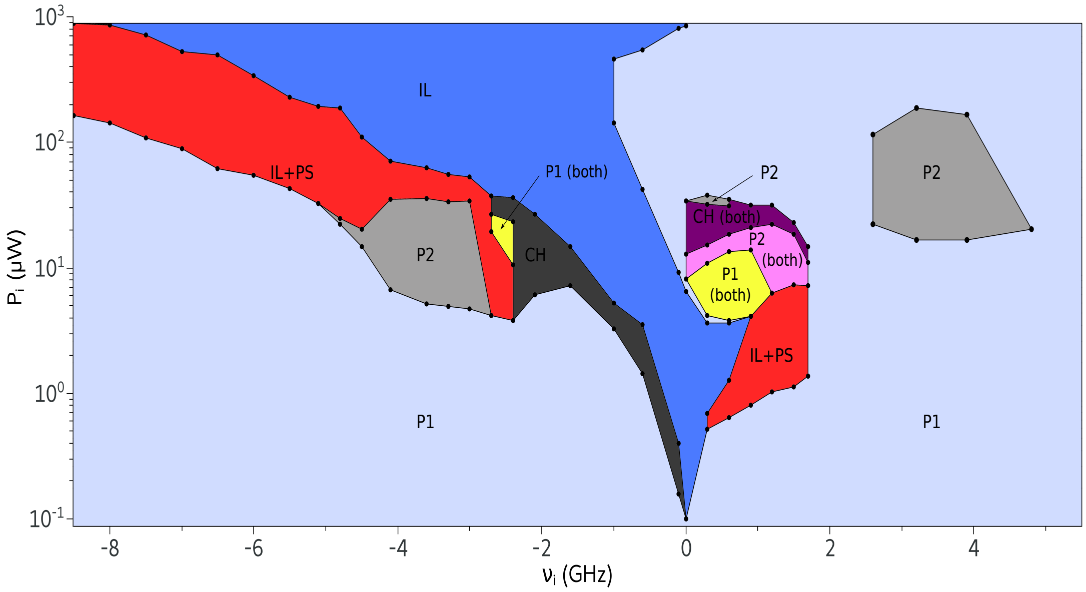

(a) Increasing P_{inj}

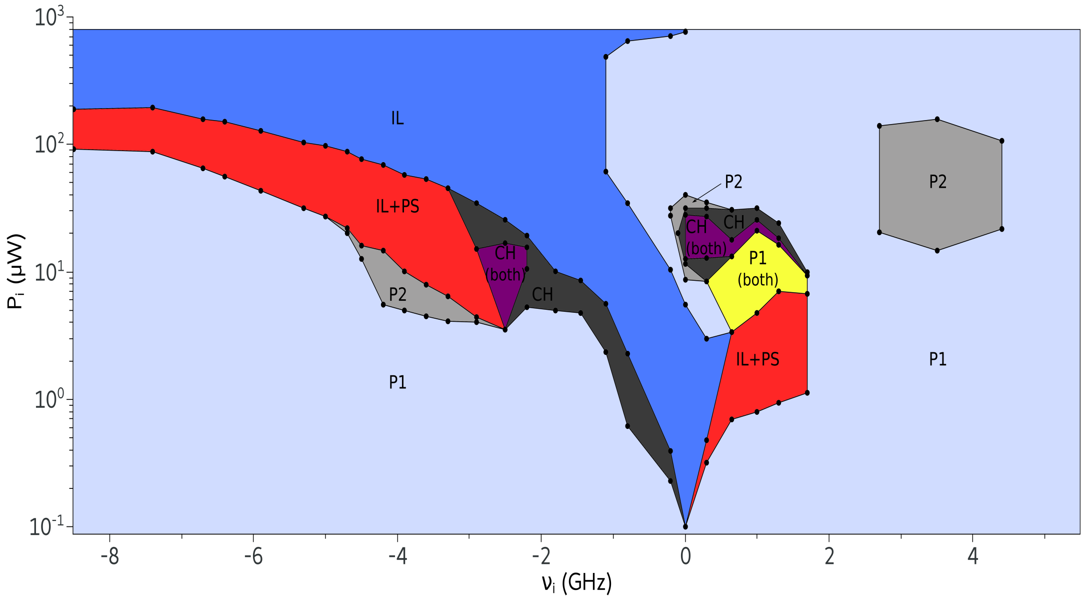

(b) Decreasing P_{inj}

Figure 3.7: Complete map of dynamics for bias current I= 3 mA. Different regions are observed. Period 1 (P1), period 2 (P2), chaos (CH), injection locking (IL), injection locking and polarization switching (IL+PS), period 1 in both polarizations (P1 both), period 2 in both polarizations (P2 both) and chaos in both polarizations (CH both)

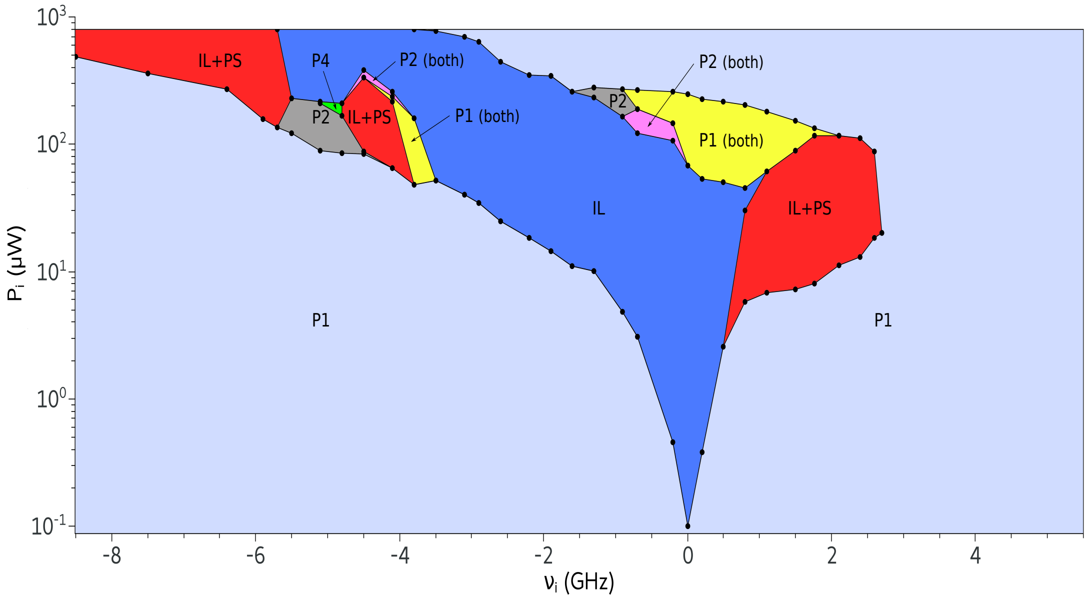

(a) Increasing P_{inj}

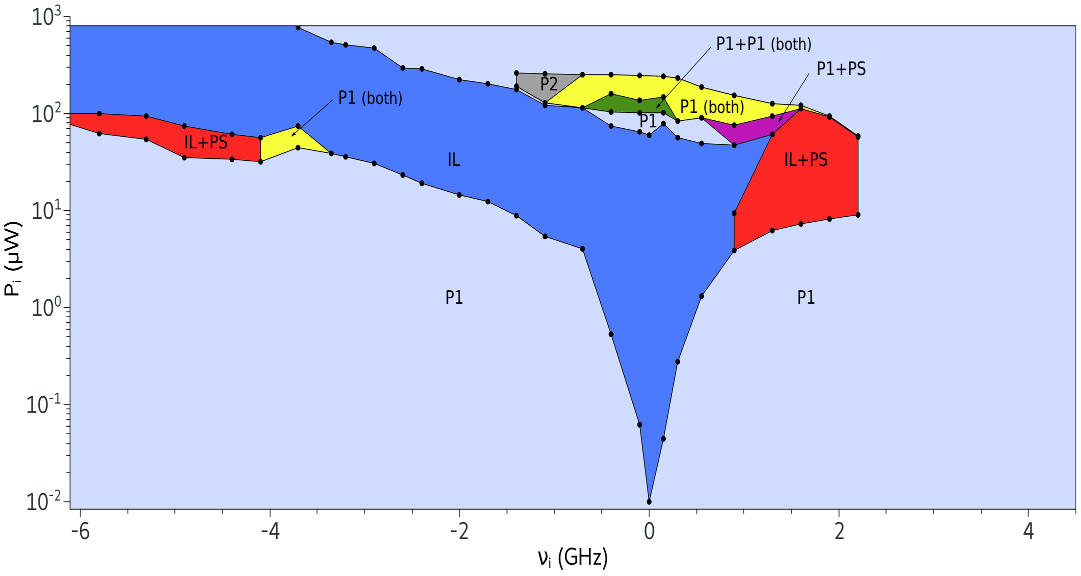

(b) Decreasing P_{inj}

Figure 3.8: Complete map of dynamics for bias current I= 5 mA. Different regions are observed. Period 1 (P1), period 2 (P2), period 4 (P4), injection locking (IL), injection locking and polarization switching (IL+PS), period 1 in both polarizations (P1 both), period 2 in both polarizations (P2 both), switching in time between two periodic behaviours P2+P1 both (period doubling P2 and limit cycle appearing simultaneously in both polarization P1 both) and a switching in time between period 1 in the parallel polarization and polarization switching (P1+PS)

3.3.2 Optical Spectra & Time Traces

The time traces are obtained simultaneously using two different high-speed detectors (9 GHz). The detector used to get the orthogonal signal presents a delay of 0.4 ns with regards to the one used to measure the parallel traces, that has been compensated on the graphs. The signals have been scaled to compensate both the differences between the two detectors and the signal losses induced by the polarization beam splitter, and the parallel signal was shifted from 0.017 (a.u) in order to avoid overlapping of parallel and orthogonal signals. The black time traces correspond to the parallel polarization signal, and blue traces correspond to orthogonal polarization signal.

We give in figure 3.9 the spectra of very well known regions, appearing consecutively when increasing the level of injection for a constant detuning $\nu_i = -3.5$ GHz, for a bias current I = 3 mA. We give respectively in figure 3.9(a) the limit cycle (P1) at the detuning frequency, in figure 3.9(b) the period doubling (P2), which temporal series is given in figure 3.11(a). In figure 3.9(c) injection locking and polarization switching obtained simultaneously (IL+PS) and in figure 3.9(d) the injection locking state (IL).

(a) P1 : $P_{inj} = 0.932\ \mu$W (b) P2 : $P_{inj} = 5.82\ \mu$W

(c) IL+PS : $P_{inj} = 38.88\ \mu$W (d) IL : $P_{inj} = 93.52\ \mu$W

Figure 3.9: Spectra for different regions (a) - P1, (b) - P2, (c) - IL+PS and (d) - IL for a bias current $I = 3$ mA, and a detuning $\nu_i = -3.5$ GHz, when increasing the injected power

We also give in figure 3.10(a) and 3.10(b) two chaotic behaviours obtained when decreasing the level of injection for a fixed detuning $\nu_i = -2.2$ GHz, and a bias current I = 3 mA.

(a) CH : $P_{inj} = 19.87\ \mu$W (b) CH both : $P_{inj} = 14.21\ \mu$W

Figure 3.10: Spectra for different regions (a) - CH and (b) - CH both for a bias current $I = 3$ mA, and a detuning $\nu_i = -2.2$ GHz, when decreasing the injected power

The chaotic behaviour in the parallel polarization is a well known state that has been characterized [20] and we give in figure 3.11(b) its temporal trace. However the chaotic behaviour appearing simultaneously in both polarization modes (spectrum figure 3.10(b)) is a really new state, and we give its time series in figure 3.11(c). This state is characterized by a broadened spectrum in both polarization modes, and by an aperiodic time trace in both polarizations.

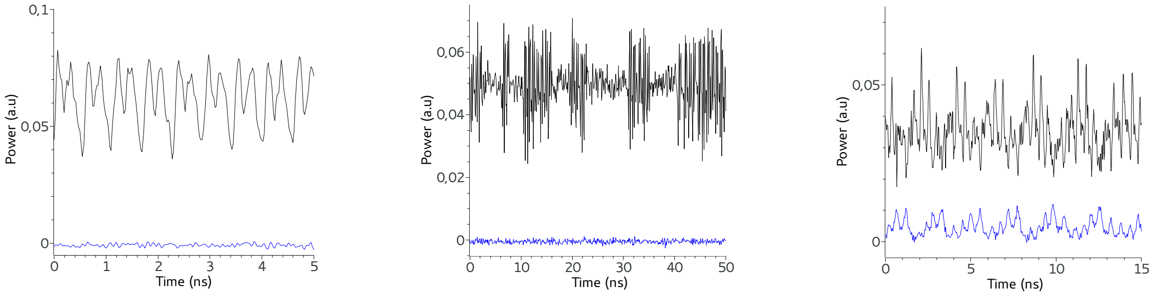

(a) P2 (b) CH (c) CH (both)

Figure 3.11: Time traces for some behaviours : P2, CH and CH (both) corresponding respectively to the spectra on figures 3.9(b), 3.10(a) and 3.10(b). Black is the parallel signal and blue the the orthogonal signal. Traces have been shifted in order to avoid overlapping

The figure 3.12 gives the spectra of four non-linear behaviours appearing consecutively when increasing the level of injected power at a fixed detuning $\nu_i = 0.7$ GHz, and a fixed bias current I = 3 mA. Figure 3.12(a) is the IL+PS state, figure 3.12(b) is the simultaneous appearance in both polarizations of a limit cycle (P1 both) at the relaxation oscillation frequency (2 GHz), figure 3.12(c) is a period doubling occurring simultaneously in both polarization modes, and finally figure 3.12(d) is a chaotic behaviour appearing in both polarizations.

(a) IL+PS : $P_{inj} = 0.971$ μW (b) P1 both : $P_{inj} = 3.88$ μW

(c) P2 both : $P_{inj} = 13.29$ μW (d) CH both : $P_{inj} = 17.06$ μW

Figure 3.12: Spectra for different regions. (a) - IL+PS, (b) - P1 both, (c) - P2 both, and (d) - CH both for $I = 3$ mA, and a detuning $\nu_i = 0.7$ GHz, when increasing $\mathrm{P_{inj}}$

These behaviours occurring simultaneously in both polarizations modes are really new, and we clearly see the root to chaos (fixed point, limit cycle, period doubling, chaos) appearing in both polarizations, that could be shown in a bifurcation diagram.

We give also in figure 3.13 the time traces corresponding to these non-linear behaviours (P1 both, P2 both, CH both). In these time traces, we see clearly that there is noise for the periodic behaviours, and we would not have seen the period doubling, which is 15 dB weaker, without the optical spectrum analyser.

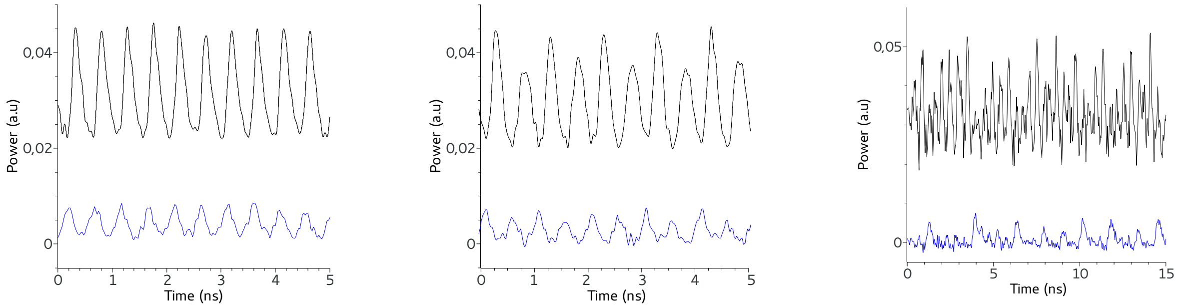

(a) P1 (both) (b) P2 (both) (c) CH (both)

Figure 3.13: Time traces for some behaviours : P1 (both),P2 (both) and CH (both) corresponding respectively to the spectra on figures 3.12(b), 3.12(c) and 3.12(d). Black is the parallel signal and blue the the orthogonal signal. Traces have been shifted in order to avoid overlapping

In figure 3.14 are given a panel of non-linear dynamics for a bias current I = 5 mA and various values of the detuning. In figure 3.14(a) is given an example of period quadrupling (P4) in the parallel polarization that has been obtained for the first time with this VCSEL, for a detuning $\nu_i = -5$ GHz, when increasing the level of injected power. In figure 3.14(b) is given an example of limit cycle occurring simultaneously in both polarizations (P1 both), for a detuning $\nu_i = -3.6$ GHz, when increasing P_{inj}. And finally in figures 3.14(c) and 3.14(d) are given two very new behaviours, that are asymmetrical : P1+P1 both and P1+PS. These behaviours can be explained with the time series that we give bellow.

(a) P4 : $P_{inj} = 182.9\ \mu$W, $\nu_i = -5$ GHz, increasing injected power

(b) P1 both : $P_{inj} = 58.64\ \mu$W, $\nu_i = -3.6$ GHz, increasing injected power

(c) P2+P1 both : $P_{inj} = 155.3\ \mu$W, $\nu_i = -0.4$ GHz, decreasing injected power

(d) P1+PS : $P_{inj} = 59.71\ \mu$W, $\nu_i = 1.1$ GHz, decreasing injected power

Figure 3.14: Spectra for different regions (a) - P4, (b) - P1 both, (c) - P2+P1 both and (d) - P1+PS for a bias current $I = 5$ mA, and various values of detuning

Are given in figures 3.15(a) to 3.15(c) the time series corresponding to the limit cycle P1, the period doubling P2 and the period quadrupling P4 which spectrum is given in figure 3.14(a). These time traces have been obtained for a fixed value of the detuning, when increasing the level of injection P_{inj}. We can clearly see the period doubling cascade occurring when increasing the injection parameter.

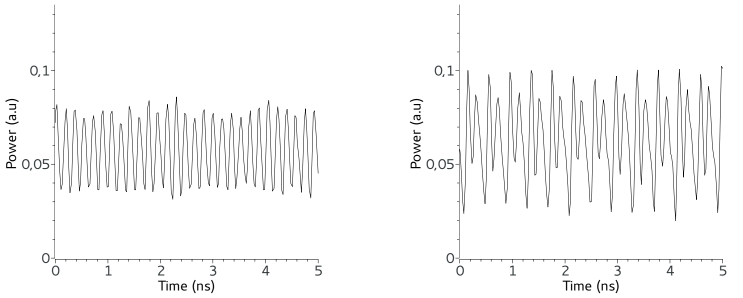

(a) P1 (b) P2 (c) P4

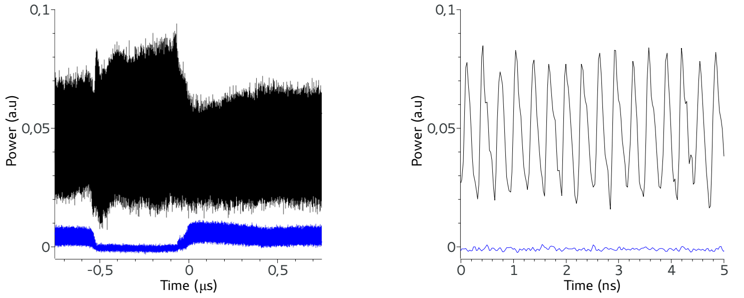

(d) P2+P1(both) (e) P2+P1(both) : P1 (f) P2+P1(both) : P1(both)

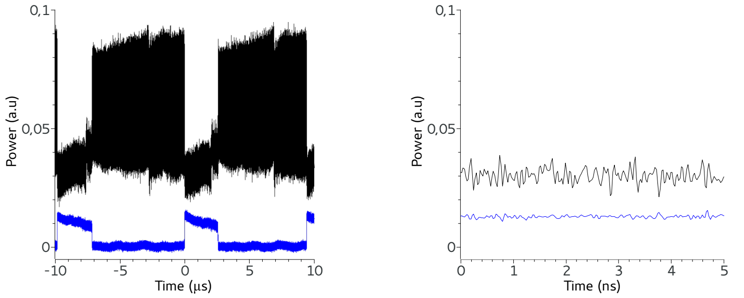

(g) P1+PS (h) P1+PS : Zoom IL+PS (i) P1+PS : Zoom P1

Figure 3.15: Time traces for some behaviours : P4, P1+P1 both and P1+PS. Figures (a) to (c) show the period doubling cascade from P1 to P4 (corresponding to figure 3.14(a)). Figures (d) to (f) show that P2+P1 both (spectra figure 3.14(c)) is a switching between a P2 (e) and a P1 (both) (f). Figures (g) to (i) show that P1+PS (spectra figure 3.14(d)) is a switching between a IL+PS (h) and a P1 (i). Black is the parallel signal and blue the the orthogonal signal. Traces have been shifted in order to avoid overlapping

In figures 3.15(d) to 3.15(f), we explore the new behaviour (P2+P1 both), which spectrum is given in figure 3.14(c). The spectrum analysis gives that P1 (P2) is close to the relaxation oscillation frequency 3.1 GHz (1.5 GHz). The study of the time series allows us to analyse this behaviour. It results from an aperiodic switching, on a microsecond time scale, between two stable states : P2 (zoom figure 3.15(e)) and a P1 both (3.15(f)). In a similar manner, P1+PS (spectrum 3.14(d)) results from a switching between IL+PS (3.15(h)) and P1 (3.15(i)) at the relaxation oscillation frequency 3.1 GHz.

4 Two-State Intermittency & Multistability

We focus in this section on the region of the maps given in figures 3.8(b) where a two-state intermittency has been observed. We give a more precise map where various cases of intermittency can be found. The reason some of the states that are going to be presented here are not in the maps of the figure 3.8 is that these maps have been obtained only by looking to the experimental optical spectra, and the spectra of some of these *new* states are exactly the same than the optical spectra of other states.

4.1 Mapping of the Multistable Regions

We present in this section the mapping of the hopping behaviours that appear at positive frequency detuning values, for a bias current $I_{\text{bias}} = 5.0$ mA, and when decreasing the level of injection. In this map, given in figure 4.1(a), new dynamical situations are presented. These states result from the switching between two, or more, stable states. Indeed, the region we are focusing on is highly multistable, which means that more than two attractors coexist in this region.

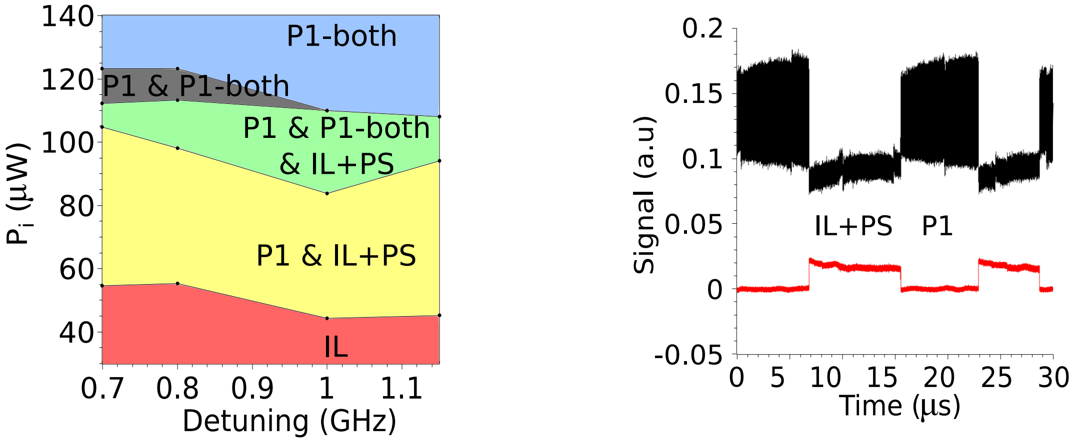

(a) Map of multistability (b) P1 & IL+PS time trace

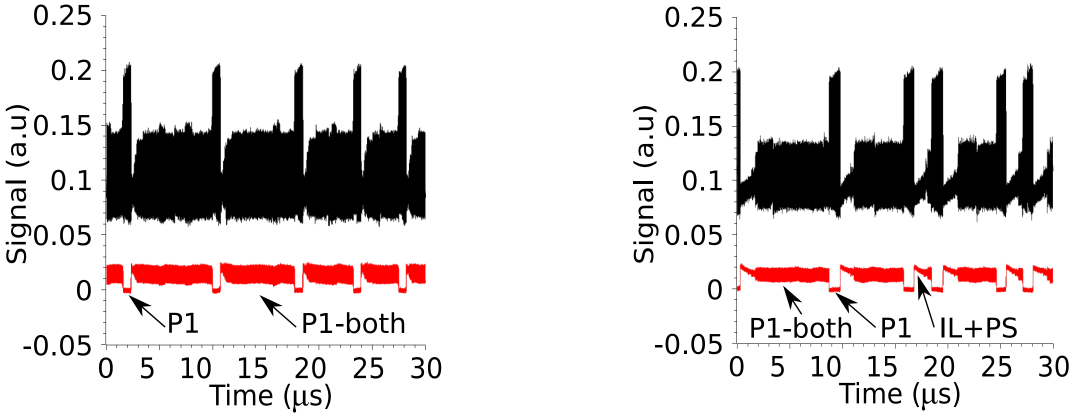

(c) P1 & P1-both time trace (d) P1 & P1-both & IL+PS time trace

Figure 4.1: (a) Precise mapping of the region where multistability is observed, for bias current 5.0 mA when decreasing the level of injection. (b), (c) and (d) Time series of the (P1 & IL+PS) state, (P1 & P1-both) state and (P1 & P1-both & IL+PS) state, obtained for $\nu_i = 0.9$ GHz $P_i = 53.83$ μW, $\nu_i = 0.7$ GHz $P_i = 127.0$ μW, and $\nu_i = 0.9$ GHz $P_i = 106.2$ μW respectively. Black (red) is the parallel (orthogonal) polarization signal.

We see in this map that three intermittent behaviours can be found. First the P1+PS, or (P1 & IL+PS), where the system jumps between the P1 state and the IL+PS state, which time trace is given in figure 4.1(b). This state will be closely studied in the following section, in particular with regards to its temporal traces, residence time distributions, etc. Secondly, another two-state intermittency has been found where the system switches between the P1 state and the P1-both state. The time series of this state is given in figure 4.1(c). This time trace shows that the two-state intermittency is aperiodic, and this aperiodicity will be discussed in the case of the (P1 & IL+PS) state. It is to be noted that the optical spectrum of this state is really similar to the optical spectrum of the P1-both state.

Finally, a state where the system is hopping between three attractors is observed for a small region of the map. Its time trace is given in figure 4.1(d). First, it is to be noted that the optical spectrum of this state is, again, really similar to the optical spectrum of the P1-both state. Secondly, we see in this time trace that the attractor hopping follow a sequence, that is P1, then IL+PS, then P1-both. The system never jumps from P1-both to IL+PS for instance. This sequence is counter-intuitive in a three potential-well system, and has not been observed in other multistate hopping dynamics in our knowledge [24–26]. We also give in figure 4.2 a representation of the attractors in the orthogonal-parallel polarization power plane. This representation shows the three states, and the arrows show the sequence of hopping. The ellipse given by the P1-both state, that is really compressed, shows that the two oscillating orthogonal polarizations are anticorrelated.

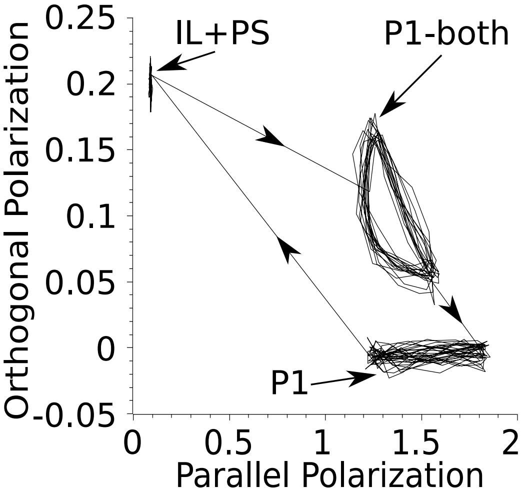

Figure 4.2: Representation of the three attractors, that are P1, P1-both, and IL+PS, in the orthogonal-parallel polarization power plane. The ellipse is the P1-both attractor, the P1 attractor is when the orthogonal polarization is suppressed and the parallel oscillates, and the IL+PS state is a point where both polarizations are constant at a positive value. The arrows show the sequence of the attractor hopping.

We will now focus on the analysis of long time series of the (P1 & IL+PS) state, in order to characterize the hopping mechanism. This two-state intermittency is not really well understood and many interpretations can be advanced, including on-off intermittency, coherence resonance, etc.

4.2 Analysis of the P1+PS State - Time Series

We focus more specifically, in this section, on the behaviour (P1 & IL+PS) and we characterize the switching between P1 and IL+PS. Note that a similar study could be done on the (P2 & P1-both) region, or on the (P1 & P1-both) region. We give on figure 4.3 a view of a time series for the (P1 & IL+PS) behaviour on a very large time scale, and then consecutive zooms. We only plot the orthogonal polarization signal for clarity purposes, and therefore when the signal is at its smaller (respectively higher) values, the system is on the P1 state (respectively IL+PS state).

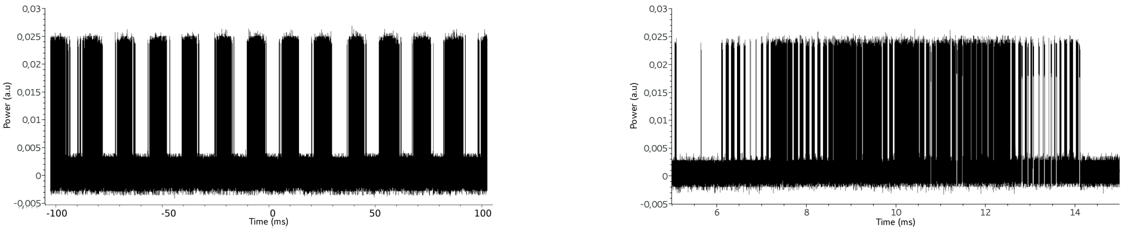

(a) Complete time scale (b) Zoom on one of the peaks

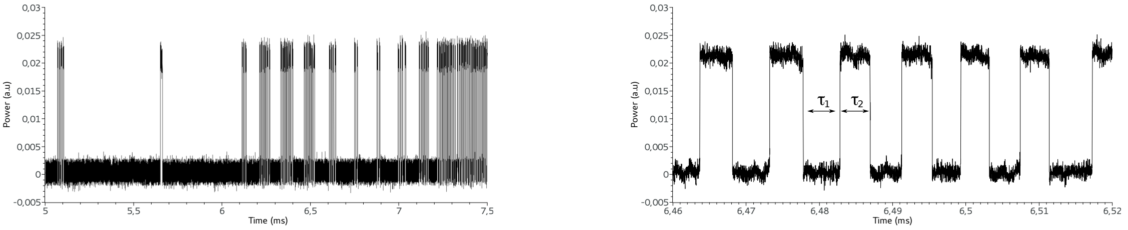

(c) Zoom on a small time scale (d) Zoom on some consecutive switches

Figure 4.3: Time trace of a P1+PS behaviour obtained for $\nu_i = 0.9$ GHz and $P_{\text{inj}} = 72.7\ \mu$W. We only plot the orthogonal polarization for clarity purposes. Figure (a) shows the complete time trace, and figures (b) to (d) are consecutive zooms of this time trace. We define the residence time τ_1 (τ_2) the time the system stays on P1 (IL+PS).

This is only an example of time series and we characterized the switching in different time traces by measuring the residence time τ_1 (τ_2) corresponding to the time the system stays on P1 (IL+PS). Figure 4.4 shows the probability density function of both times ($P(\tau_i)$) for some points in the P1+PS region, in log-log scale[1]. Table 4.1 also gives the mean value and the standard deviation for the same points in the P1+PS region. The points are characterized by their injection properties that are given with this table.

Table 4.1: Mean value and standard deviation of τ_1 and τ_2 for three points of the P1+PS region, characterized by their injection parameters ν_i and P_{inj}

Injection	τ_i	Mean value	Standard Deviation
$\nu_i = 0.9$ GHz	τ_1	19.668 (μs)	232.8 (μs)
$P_{\text{inj}} = 72.7\ \mu$W	τ_2	5.145 (μs)	2.099 (μs)
$\nu_i = 1.1$ GHz	τ_1	5.458 (μs)	5.503 (μs)
$P_{\text{inj}} = 82.4\ \mu$W	τ_2	34.62 (μs)	189.6 (μs)
$\nu_i = 1.3$ GHz	τ_1	1.255 (μs)	0.255 (μs)
$P_{\text{inj}} = 86.5\ \mu$W	τ_2	11.769 (μs)	43.41 (μs)

---

[1] Was developed a software in python (with GUI) that allows you to plot these log-log *pdf*.

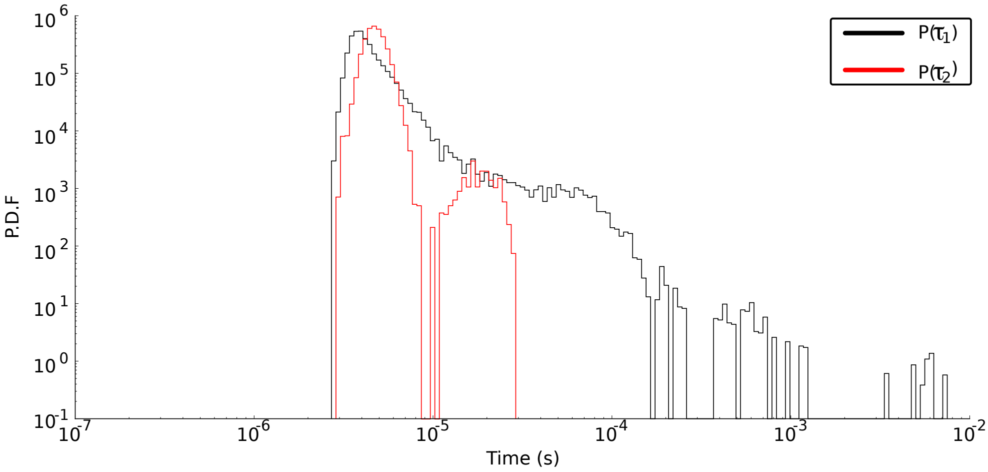

(a) *PDF* of τ_1 and τ_2 corresponding to injection parameters $\nu_i = 0.9$ GHz, $P_{\text{inj}} = 72.7\ \mu$W

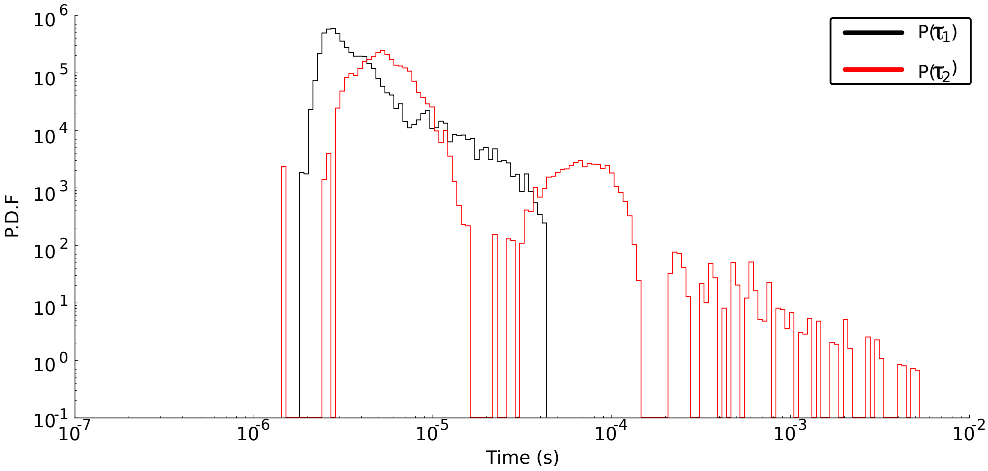

(b) *PDF* of τ_1 and τ_2 corresponding to injection parameters $\nu_i = 1.1$ GHz, $P_{\text{inj}} = 82.4\ \mu$W

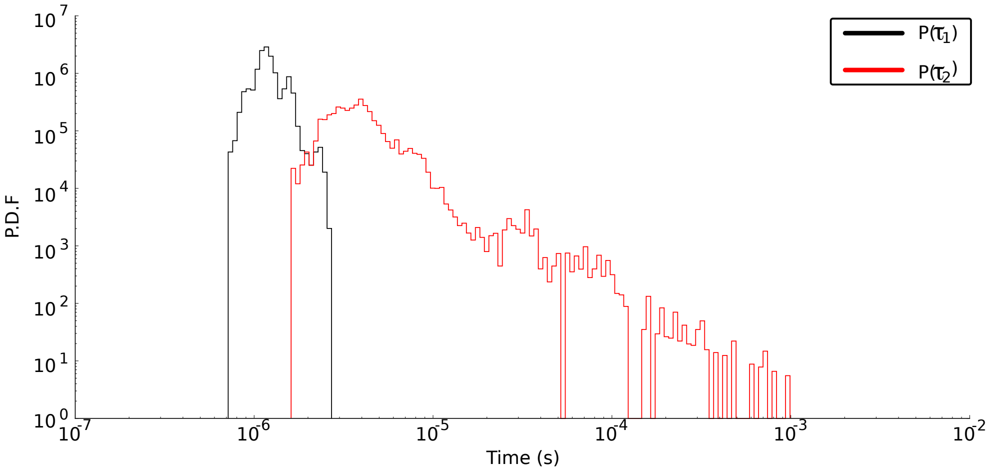

(c) *PDF* of τ_1 and τ_2 corresponding to injection parameters $\nu_i = 1.3$ GHz, $P_{\text{inj}} = 86.5\ \mu$W

Figure 4.4: Probability density function (*PDF*) of the residence times τ_1 and τ_2 for three points of the P1+PS region. The black (red) curve shows the *PDF* of the residence time τ_1 (τ_2) of the system on the P1 (IL+S) state.

These three residence time distributions present similar long-tail distributions, but in one case (figure 4.4(a)) the dominating state is P1, meaning that the system is mostly on the P1 state and jumps to the IL+PS state. In another case (figure 4.4(c)) the dominating state is IL+PS, and in the last case (figure 4.4(b)), both states present long-tail residence time distributions. We give three other cases in the panel of the figure 4.5[2]. Two cases that are close to the one presented in figures 4.4(a) and 4.4(c), and one case with a behaviour similar to coherence resonance, where the hopping dynamics is quasi periodic (center panel).

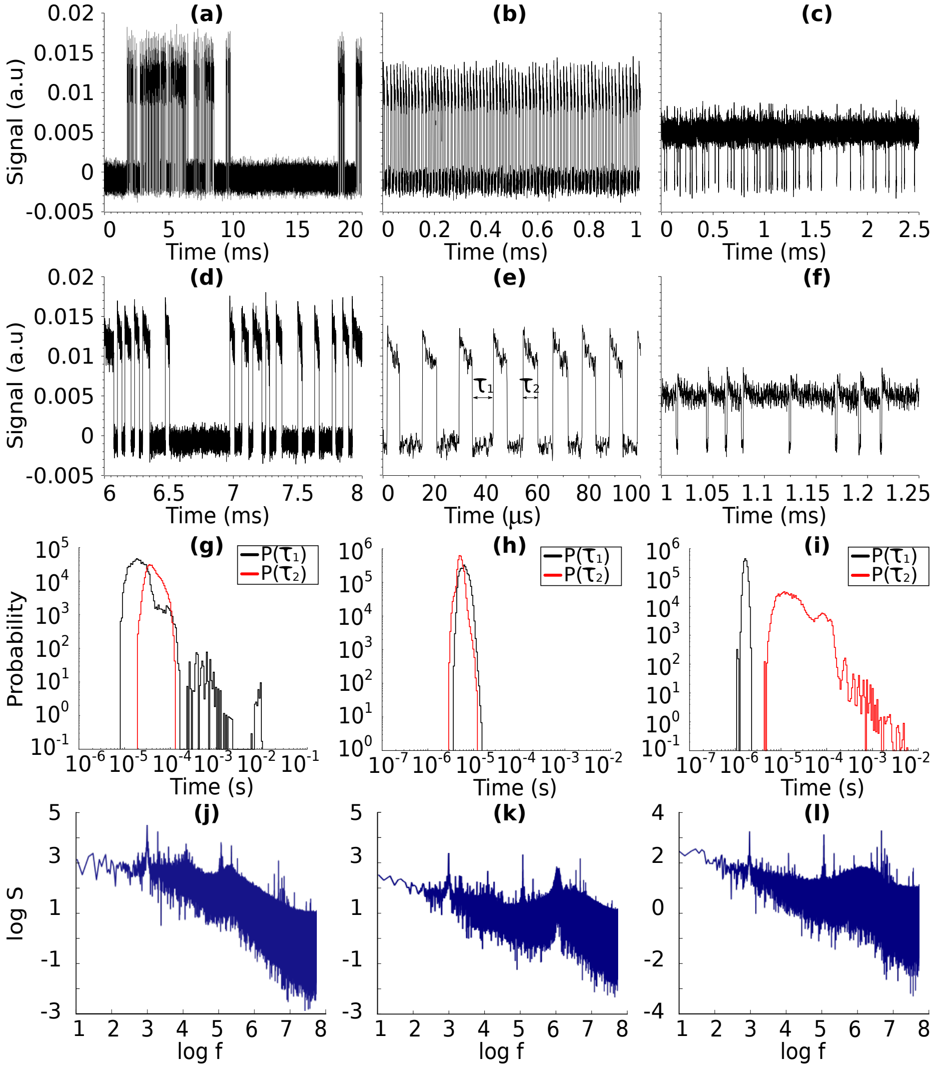

Figure 4.5: Experimental time trace of the orthogonal polarization signal of the P1 & IL+PS state **(a b c)**, zoomed parts of the time series **(d e f)**, residence time distributions in log-log scale **(g h i)**, and Fourier transforms **(j k l)**. The system is on the P1 (IL+PS) state when the signal is on its lower (higher) value, and we define the residence time on P1 (IL+PS) as τ_1 (τ_2), in black (red) in the residence time distribution figures. All measurements are done at $I_{bias} = 5$ mA. Left panel, where P1 is the dominating state, is obtained for $\nu_i = 0.8$ GHz and $P_i = 48.01$ μW. Center panel, where P1 and IL+PS are similarly distributed, is obtained for $\nu_i = 0.9$ GHz and $P_i = 53.83$ μW. And finally right panel, where IL+PS is the dominating state, is obtained for $\nu_i = 1.1$ GHz and $P_i = 64.71$ μW.

---

[2] This panel will be used in a manuscript, see Appendix D

This panel shows many things. First the time series and the residence time distributions demonstrate a coherence enhanced intermittency [26]. Indeed, in most part of the region where the (P1 & IL+PS) state can be observed, the center panel case is obtained, and close to the regions where respectively P1 or IL+PS state are stable (see figure 3.8(b)), left and right panel are obtained. Secondly, the spectra obtained by Fourier transform of the long time series for the orthogonal polarization signal, figure 4.5(j k l) show that this signal is a good example of 1/f noise signal [40–42]. A manuscript analysing these time series on a statistical point of view will be written in a near future.

⁂

Summary and Outlook

In this work, we have explored and studied the polarization dynamics of a 1550-nm VCSEL subject to parallel optical injection. We have characterized the unusual state, named IL+PS, where the locking of the parallel polarization of the VCSEL on the emitted light and an excitation of the orthogonal polarization occur simultaneously. This state is unusual because an injection in the polarization with smaller optical losses induces an excitation of the polarization with larger optical losses. More precisely, we characterized theoretically (through a linear stability analysis of the IL+PS steady state), numerically (through the numerical simulation of the spin-flip model), and experimentally the region of the injected power-frequency detuning plane where the IL+PS region can be observed. We have found a very good qualitative and quantitative agreement, nevertheless with some exceptions, mostly due to other non-linear dynamics in the system.

We also characterized the bistability induced by power variations of the master laser for a fixed value of the frequency detuning. Several types of bistability can be found, and we focused our work on two of them. First the bistability between the IL+PS region and the limit cycle found below the lower boundary of the IL+PS region. And secondly the bistability between the IL+PS region and the IL region found above the higher boundary of the IL+PS region for negative values of the frequency detuning. This bistability has been confirmed theoretically by performing the linear stability analysis of the IL+PS state, and the IL state. Very good qualitative and quantitative agreement is found. These characterizations of the IL+PS region have been performed for several bias currents, respectively 3.0 mA, 4.0 mA, and 5.0 mA.

We finally presented a mapping of the various non-linear behaviours found in this VCSEL subject to parallel optical injection. These non-linear behaviours are of two types. First a large variety of behaviours in which only the parallel polarization is excited. For instance limit cycle (P1), period doubling (P2) and quadrupling (P4), and chaos (CH). These behaviours have been widely explored in many papers. And secondly some behaviours in which both polarizations are involved. For instance periodic behaviours occurring simultaneously in both polarizations (P1-both, P2-both), chaotic behaviours appearing in both polarizations (CH-both). Finally, dynamics resulting from a switching between two stable states are observed. We found and studied, in particular, a state resulting from a switching between a periodic solution in the parallel polarization and the IL+PS state, a switching between P2 and P1-both, a switching between P1 and P1-both, and even a multistate hopping between IL+PS, P1 and P1-both. We also think from recent results that a state resulting from a switching between IL and CH has also been observed.

The characterization of these hopping dynamics is still in progress and drives a real interest, both regarding the physical mechanism leading to the attractor hopping, that can be due to a thermal effect or a noise induced coherence intermittency [26], and regarding the theoretical analysis of the temporal series in the view of 1/f noise classification [41,42].

A more precise conclusion on these different points can be found in the conclusions of the manuscripts that have been written in parallel of this work, and that are presented in appendix D.

References

[1] F. Koyama, "Recent advances of VCSEL photonics," *Journal of Lightwave Technology*, vol. 24, no. 12, pp. 4502–4513, 2006.

[2] R. Michalzik, *VCSELs: fundamentals, technology and applications of vertical-cavity surface-emitting lasers*, vol. 166. Springer, 2012.

[3] M. San Miguel, Q. Feng, and J. V. Moloney, "Light-polarization dynamics in surface-emitting semiconductor lasers," *Phys. Rev. A*, vol. 52, pp. 1728–1739, Aug 1995.

[4] A. Valle, L. Pesquera, and K. Shore, "Polarization behavior of birefringent multi-transverse mode vertical-cavity surface-emitting lasers," *IEEE Photonics Technology Letters*, vol. 9, no. 5, pp. 557–559, 1997.

[5] K. Panajotov, B. Ryvkin, J. Danckaert, M. Peeters, H. Thienpont, and I. Veretennicoff, "Polarization switching in VCSEL's due to thermal lensing," *IEEE Photonics Technology Letters*, vol. 10, no. 1, pp. 6–8, 1998.

[6] T. Simpson, J. Liu, and A. Gavrielides, "Bandwidth enhancement and broadband noise reduction in injection-locked semiconductor lasers," *IEEE Photonics Technology Letters*, vol. 7, no. 7, pp. 709–711, 1995.

[7] L. Chrostowski, B. Faraji, W. Hofmann, M.-C. Amann, S. Wieczorek, and W. W. Chow, "40 GHz bandwidth and 64 GHz resonance frequency in injection-locked 1.55 μm VCSELs," *IEEE Journal of Selected Topics in Quantum Electronics*, vol. 13, no. 5, pp. 1200–1208, 2007.

[8] Y. Hong, K. Shore, A. Larsson, M. Ghisoni, and J. Halonen, "Polarisation switching in a vertical cavity surface emitting semiconductor laser by frequency detuning," *IEEE Proceedings-Optoelectronics*, vol. 148, no. 1, pp. 31–34, 2001.

[9] J. B. Altés, I. Gatare, K. Panajotov, H. Thienpont, and M. Sciamanna, "Mapping of the dynamics induced by orthogonal optical injection in vertical-cavity surface-emitting lasers," *IEEE Journal of Quantum Electronics*, vol. 42, no. 2, pp. 198–207, 2006.

[10] K. H. Jeong, K. H. Kim, S. H. Lee, M. H. Lee, B.-S. Yoo, and K. A. Shore, "Optical injection-induced polarization switching dynamics in 1.5-μm wavelength single-mode vertical-cavity surface-emitting lasers," *IEEE Photonics Technology Letters*, vol. 20, no. 10, pp. 779–781, 2008.

[11] A. Hurtado, I. D. Henning, and M. J. Adams, "Two-wavelength switching with a 1550 nm VCSEL under single orthogonal optical injection," *IEEE Journal of Selected Topics in Quantum Electronics*, vol. 14, no. 3, pp. 911–917, 2008.

[12] A. Quirce, P. Pérez, A. Popp, Ángel Valle, L. Pesquera, Y. Hong, H. Thienpont, and K. Panajotov, "Polarization switching and injection locking in vertical-cavity surface-emitting lasers subject to parallel optical injection," *Opt. Lett.*, vol. 41, pp. 2664–2667, Jun 2016.

[13] H. Kawaguchi, "Bistable laser diodes and their applications: state of the art," *IEEE Journal of Selected Topics in Quantum Electronics*, vol. 3, no. 5, pp. 1254–1270, 1997.

[14] Z. G. Pan, S. Jiang, M. Dagenais, R. A. Morgan, K. Kojima, M. T. Asom, R. E. Leibenguth, G. D. Guth, and M. W. Focht, “Optical injection induced polarization bistability in vertical-cavity surface-emitting lasers,” *Applied Physics Letters*, vol. 63, no. 22, pp. 2999–3001, 1993.

[15] T. Mori, Y. Yamayoshi, and H. Kawaguchi, “Low-switching-energy and high-repetition-frequency all-optical flip-flop operations of a polarization bistable vertical-cavity surface-emitting laser,” *Applied Physics Letters*, vol. 88, no. 10, p. 101102, 2006.

[16] J. Sakaguchi, T. Katayama, and H. Kawaguchi, “All-optical memory operation of 980-nm polarization bistable VCSEL for 20-Gb/s PRBS RZ and 40-Gb/s PRBS NRZ data signals,” *Optics Express*, vol. 18, no. 12, pp. 12362–12370, 2010.

[17] T. Katayama, D. Hayashi, and H. Kawaguchi, “All-optical shift register using polarization bistable VCSEL array,” *IEEE Photonics Technology Letters*, vol. 28, no. 19, pp. 2062–2065, 2016.

[18] S. H. Lee, H. W. Jung, K. H. Kim, M. H. Lee, B.-S. Yoo, J. Roh, and K. A. Shore, “1-GHz all-optical flip-flop operation of conventional cylindrical-shaped single-mode VCSELs under low-power optical injection,” *IEEE Photonics Technology Letters*, vol. 22, no. 23, pp. 1759–1761, 2010.

[19] T. Katayama, K. Nakao, D. Hayashi, and H. Kawaguchi, “Flip-flops using polarization bistable VCSEL with AND-gate functionality by two wavelength inputs,” *IEICE Electronics Express*, vol. 13, no. 5, pp. 1–6, 2016.

[20] S. Wieczorek, B. Krauskopf, T. Simpson, and D. Lenstra, “The dynamical complexity of optically injected semiconductor lasers,” *Physics Reports*, vol. 416, no. 1, pp. 1–128, 2005.

[21] A. Hurtado, A. Quirce, A. Valle, L. Pesquera, and M. J. Adams, “Nonlinear dynamics induced by parallel and orthogonal optical injection in 1550 nm vertical-cavity surface-emitting lasers (vcsels),” *Optics express*, vol. 18, no. 9, pp. 9423–9428, 2010.

[22] R. Al-Seyab, K. Schires, N. A. Khan, A. Hurtado, I. D. Henning, and M. J. Adams, “Dynamics of polarized optical injection in 1550-nm vcsels: theory and experiments,” *Selected Topics in Quantum Electronics, IEEE Journal of*, vol. 17, no. 5, pp. 1242–1249, 2011.

[23] T. Simpson, J. Liu, K. Huang, and K. Tai, “Nonlinear dynamics induced by external optical injection in semiconductor lasers,” *Quantum and Semiclassical Optics: Journal of the European Optical Society Part B*, vol. 9, no. 5, p. 765, 1997.

[24] S. Kim, S. H. Park, and C. S. Ryu, “Noise-enhanced multistability in coupled oscillator systems,” *Physical review letters*, vol. 78, no. 9, p. 1616, 1997.

[25] G. Huerta-Cuellar, A. N. Pisarchik, and Y. O. Barmenkov, “Experimental characterization of hopping dynamics in a multistable fiber laser,” *Physical Review E*, vol. 78, no. 3, p. 035202, 2008.

[26] A. Campos-Mejia, A. Pisarchik, R. Sevilla-Escoboza, G. Huerta-Cuellar, and V. Vera-Avila, “Coherence enhanced intermittency in an optically injected semiconductor laser,” *Optics express*, vol. 23, no. 8, pp. 10428–10434, 2015.

[27] M. A. Arteaga, M. Valencia, M. Sciamanna, H. Thienpont, M. López-Amo, and K. Panajotov, “Experimental evidence of coherence resonance in a time-delayed bistable system,” *Physical review letters*, vol. 99, no. 2, p. 023903, 2007.

[28] G. Friart, A. Gavrielides, and T. Erneux, “Analytical stability boundaries of an injected two-polarization semiconductor laser,” *Physical Review E*, vol. 91, no. 4, p. 042918, 2015.

[29] T. Maiman, “Stimulated emission from a ruby crystal,” 1960.

[30] M.-R. Park, O.-K. Kwon, W.-S. Han, K.-H. Lee, S.-J. Park, and B.-S. Yoo, “All-monolithic 1.55 μm inalgaas/inp vertical cavity surface emitting lasers grown by metal organic chemical vapor deposition,” *Japanese journal of applied physics*, vol. 45, no. 1L, p. L8, 2005.

[31] P. Pérez, A. Valle, I. Noriega, and L. Pesquera, “Measurement of the intrinsic parameters of single-mode vcsels,” *Journal of Lightwave Technology*, vol. 32, no. 8, pp. 1601–1607, 2014.

[32] A. P. Popp, “Polarisation of vertical-cavity surfaceemitting lasers (vcsels) subject to parallel optical injection,” *Universidad de Cantabria - Trabajo de Fin de Grado*, 2016.

[33] J. Ohtsubo, *Semiconductor lasers: stability, instability and chaos*, vol. 111. Springer, 2008.

[34] P. Pérez, A. Valle, and L. Pesquera, “Polarization-resolved characterization of long-wavelength vertical-cavity surface-emitting laser parameters,” *JOSA B*, vol. 31, no. 11, pp. 2574–2580, 2014.

[35] M. Van Exter, M. Willemsen, and J. Woerdman, “Polarization fluctuations in vertical-cavity semiconductor lasers,” *Physical Review A*, vol. 58, no. 5, p. 4191, 1998.

[36] M. Willemsen, M. Khalid, M. Van Exter, and J. Woerdman, “Polarization switching of a vertical-cavity semiconductor laser as a kramers hopping problem,” *Physical review letters*, vol. 82, no. 24, p. 4815, 1999.

[37] M. Willemsen, M. Van Exter, and J. Woerdman, “Anatomy of a polarization switch of a vertical-cavity semiconductor laser,” *Physical review letters*, vol. 84, no. 19, p. 4337, 2000.

[38] P. Mandel and T. Erneux, “Laser lorenz equations with a time-dependent parameter,” *Physical Review Letters*, vol. 53, no. 19, p. 1818, 1984.

[39] S. Osborne, K. Buckley, A. Amann, and S. O’Brien, “All-optical memory based on the injection locking bistability of a two-color laser diode,” *Opt. Express*, vol. 17, pp. 6293–6300, Apr 2009.

[40] F. Arecchi and F. Lisi, “Hopping mechanism generating 1/f noise in nonlinear systems,” *Physical Review Letters*, vol. 49, no. 2, p. 94, 1982.

[41] M. A. Rodríguez, "Complete spectral scaling of time series: Towards a classification of 1/f noise," *Physical Review E*, vol. 90, no. 4, p. 042122, 2014.

[42] M. A. Rodríguez, "Class of perfect 1/f noise and the low-frequency cutoff paradox," *Physical Review E*, vol. 92, no. 1, p. 012112, 2015.

[43] H. Zeghlache, P. Mandel, and C. Van den Broeck, "Influence of noise on delayed bifurcations," *Physical Review A*, vol. 40, no. 1, p. 286, 1989.

[44] A. Valle, L. Pesquera, and M. Rodriguez, "Transient statistics for a good-cavity laser with swept losses," *Physical Review A*, vol. 45, no. 7, p. 5243, 1992.

A Calculations : Steady-State of the Rate Equations

In this appendix, we give the mathematical steps for the study of the steady-state of the spin-flip model (equations (1.10) and (1.7) to (1.9)).

$$
\begin{aligned}
\frac{\mathrm{d}E_x}{\mathrm{d}t} &= -(\kappa+\gamma_a)E_x - i(\kappa\alpha+\gamma_p)E_x + \kappa(1+i\alpha)(DE_x + inE_y) + \kappa E_{inj}e^{i2\pi\nu_{inj}t} \\
\frac{\mathrm{d}E_y}{\mathrm{d}t} &= -(\kappa-\gamma_a)E_y - i(\kappa\alpha-\gamma_p)E_y + \kappa(1+i\alpha)(DE_y - inE_x) \\
\frac{\mathrm{d}D}{\mathrm{d}t} &= -\gamma\left[D(1+|E_x|^2+|E_y|^2) - \mu + in(E_yE_x^* - E_xE_y^*)\right] \\
\frac{\mathrm{d}n}{\mathrm{d}t} &= -\gamma_s n - \gamma\left[n(|E_x|^2+|E_y|^2) + iD(E_yE_x^* - E_xE_y^*)\right]
\end{aligned}
$$

We write :

$$
\begin{aligned}
E_x(t) &= A_x(t)\ \exp\left(i(2\pi\nu_{inj}t + \phi_x(t))\right) \\
E_y(t) &= A_y(t)\ \exp\left(i(2\pi\nu_y t + \phi_y(t))\right) \\
\frac{\mathrm{d}E_x}{\mathrm{d}t} &= \exp\left(i(2\pi\nu_{inj}t + \phi_x(t)\right)\left[\dot{A}_x + iA_x(2\pi\nu_{inj} + \dot{\phi}_x)\right] \\
\frac{\mathrm{d}E_y}{\mathrm{d}t} &= \exp\left(i(2\pi\nu_y t + \phi_y(t)\right)\left[\dot{A}_y + iA_y(2\pi\nu_y + \dot{\phi}_y)\right]
\end{aligned}
$$

We can modify and simplify the spin-flip model equations, with $n = 0$. We simplify respectively by $\exp\left(i(2\pi\nu_{inj}t)\right)$ and $\exp\left(i(2\pi\nu_y t + \phi_y(t))\right)$

$$
\begin{aligned}
e^{i\phi_x}\left[\dot{A}_x + iA_x(2\pi\nu_{inj} + \dot{\phi}_x)\right] &= \kappa E_{inj} - A_x e^{i\phi_x}\left((\kappa+\gamma_a) + i(\kappa\alpha+\gamma_p) - \kappa D(1+i\alpha)\right) \\
\dot{A}_y + iA_y(2\pi\nu_y + \dot{\phi}_y) &= -A_y\left((\kappa-\gamma_a) + i(\kappa\alpha-\gamma_p) - \kappa D(1+i\alpha)\right) \\
\dot{D} &= -\gamma\left[D(1+A_x^2+A_y^2) - \mu\right]
\end{aligned}
$$

We separate imaginary part from real part in these equations :

$$
\begin{aligned}
\dot{A}_x &= \kappa E_{inj}\cos(-\phi_x) + (\kappa(D-1) - \gamma_a)A_x \\
A_x(2\pi\nu_{inj} + \dot{\phi}_x) &= \kappa E_{inj}\sin(-\phi_x) - A_x((\kappa\alpha+\gamma_p) - \kappa D\alpha) \\
\dot{A}_y &= (\kappa(D-1) + \gamma_a)A_y \\
2\pi\nu_y + \dot{\phi}_y &= -(\kappa\alpha - \gamma_p) + \kappa D\alpha
\end{aligned}
$$

With $A_x > 0$ and $A_y > 0$ and the transformations of frequencies, we can give the final equations given in (1.13) to (1.17).

$$\nu_i = \nu_{inj} - \frac{\alpha\gamma_a - \gamma_p}{2\pi}$$

$$
\begin{aligned}
\dot{A}_x &= (\kappa(D-1) - \gamma_a)A_x + \kappa E_{inj}\cos\phi_x \\
\dot{A}_y &= (\kappa(D-1) + \gamma_a)A_y \\
\dot{\phi}_x &= \kappa\alpha(D-1) - 2\pi\nu_i - \alpha\gamma_a - \frac{\kappa E_{inj}}{A_x}\sin\phi_x \\
\dot{\phi}_y &= \alpha(\kappa(D-1) + \gamma_a) \\
\dot{D} &= -\gamma\left[D(1+A_x^2+A_y^2) - \mu\right]
\end{aligned}
$$

We study now the steady-state of these equations :

$$\begin{aligned}
0 &= (\kappa(D_0 - 1) - \gamma_a)A_{x,0} + \kappa E_{inj}\cos\phi_{x,0} \\
0 &= (\kappa(D_0 - 1) + \gamma_a)A_{y,0} \\
0 &= \kappa\alpha(D_0 - 1) - 2\pi\nu_i - \alpha\gamma_a - \frac{\kappa E_{inj}}{A_{x,0}}\sin\phi_{x,0} \\
0 &= \alpha(\kappa(D_0 - 1) + \gamma_a) \\
0 &= -\gamma\left[D_0(1 + A_{x,0}^2 + A_{y,0}^2) - \mu\right]
\end{aligned}$$

While $A_{x,0} > 0$ and $A_{y,0} > 0$, we have :

$$\begin{aligned}
D_0 &= 1 - \frac{\gamma_a}{\kappa} \\
A_{x,0} &= \frac{\kappa E_{inj}}{2\gamma_a}\cos\phi_{x,0} \\
A_{x,0} &= -\frac{\kappa E_{inj}}{2(\pi\nu_i + \gamma_a\alpha)}\sin\phi_{x,0} \\
P_x + P_y = A_{x,0}^2 + A_{y,0}^2 &= \frac{\mu}{1 - \frac{\gamma_a}{\kappa}} - 1
\end{aligned}$$

We can obtain :

$$\begin{aligned}
\tan\phi_{x,0} &= -\left(\frac{\pi\nu_i}{\gamma_a} + \alpha\right) \\
P_{inj} &= E_{inj}^2 \\
4\gamma_a^2 A_{x,0}^2\left[1 + \left(\frac{\pi\nu_i}{\gamma_a} + \alpha\right)^2\right] &= \kappa^2 P_{inj}\left(\cos^2\phi_{x,0} + \sin^2\phi x, 0\right)
\end{aligned}$$

And finally we obtain the expressions for the different powers and for the phase :

$$\begin{aligned}
P_x = A_{x,0}^2 &= \left(\frac{\kappa}{2\gamma_a}\right)^2 \frac{P_{inj}}{1 + \left(\frac{\pi\nu_i}{\gamma_a} + \alpha\right)^2} \\
P_y = A_{y,0}^2 &= \frac{\mu}{1 - \frac{\gamma_a}{\kappa}} - 1 - P_x \\
\phi_{x,0} &= -\arctan\left(\frac{\pi\nu_i}{\gamma_a} + \alpha\right)
\end{aligned}$$

We could analyse the stability of this steady state. This study will be done, by doing a variable change and using the work [28]. The main results are given in section 2.2 and the mathematical steps are given in appendix B.

B Calculations : Variable Change & Stability Analysis

In this appendix, we give first the variable change from the spin-flip model to the model used in [28], and then the mathematical steps of the stability analysis.

The Spin-Flip model give the following equations, for $n = 0$.

$$\begin{aligned}
\frac{\mathrm{d}E_x}{\mathrm{d}t} &= -(\kappa+\gamma_a)E_x - i(\kappa\alpha+\gamma_p)E_x + \kappa(1+i\alpha)DE_x + \kappa E_{inj}e^{i2\pi\nu_{inj}t} \\
\frac{\mathrm{d}E_y}{\mathrm{d}t} &= -(\kappa-\gamma_a)E_y - i(\kappa\alpha-\gamma_p)E_y + \kappa(1+i\alpha)DE_y \\
\frac{\mathrm{d}D}{\mathrm{d}t} &= -\gamma\left[D(1+|E_x|^2+|E_y|^2)-\mu\right]
\end{aligned}$$

In these equations, we proceed to the following variable change :

$$\begin{aligned}
E_x &= \sqrt{2}E_1\exp(-i(\gamma_p-\alpha\gamma_a)t) \\
E_y &= \sqrt{2}E_2\exp(i(\gamma_p-\alpha\gamma_a)t) \\
D &= (2N+1)\left(1+\frac{\gamma_a}{\kappa}\right) \\
s &= 2\kappa\left(1+\frac{\gamma_a}{\kappa}\right)t
\end{aligned}$$

First we calculate the derivatives and then we identify in order to match the two models.

$$\begin{aligned}
\frac{\mathrm{d}E_x}{\mathrm{d}t} &= \sqrt{2}\exp(-i(\gamma_p-\alpha\gamma_a)t)\left[\frac{\mathrm{d}E_1}{\mathrm{d}t} - i(\gamma_p-\alpha\gamma_a)E_1\right] \\
\frac{\mathrm{d}E_y}{\mathrm{d}t} &= \sqrt{2}\exp(i(\gamma_p-\alpha\gamma_a)t)\left[\frac{\mathrm{d}E_2}{\mathrm{d}t} + i(\gamma_p-\alpha\gamma_a)E_2\right] \\
\frac{\mathrm{d}D}{\mathrm{d}t} &= 2\left(1+\frac{\gamma_a}{\kappa}\right)\frac{\mathrm{d}N}{\mathrm{d}t} \\
\frac{\mathrm{d}s}{\mathrm{d}t} &= 2\kappa\left(1+\frac{\gamma_a}{\kappa}\right)
\end{aligned}$$

We begin to identify the parameters for the last equation.

$$\dot{N} = \frac{\mathrm{d}N}{\mathrm{d}s} = \frac{\mathrm{d}N}{\mathrm{d}t}\frac{\mathrm{d}t}{\mathrm{d}s} = \frac{\mathrm{d}D}{\mathrm{d}t}\frac{1}{4\kappa\left(1+\frac{\gamma_a}{\kappa}\right)^2}$$

$$\frac{\mathrm{d}D}{\mathrm{d}t} = 4\kappa\left(1+\frac{\gamma_a}{\kappa}\right)^2\frac{\mathrm{d}N}{\mathrm{d}s} = -\gamma\left[(2N+1)\left(1+\frac{\gamma_a}{\kappa}\right)(1+2|E_1|^2+2|E_2|^2)-\mu\right]$$

$$\frac{2\kappa\left(1+\frac{\gamma_a}{\kappa}\right)}{\gamma}\frac{\mathrm{d}N}{\mathrm{d}s} = -(2N+1)(|E_1|^2+|E_2|^2) - N + \frac{\mu-\left(1+\frac{\gamma_a}{\kappa}\right)}{2\left(1+\frac{\gamma_a}{\kappa}\right)}$$

We can identify : $T = \dfrac{2\kappa\left(1+\frac{\gamma_a}{\kappa}\right)}{\gamma}$ and $P = \dfrac{\mu-\left(1+\frac{\gamma_a}{\kappa}\right)}{2\left(1+\frac{\gamma_a}{\kappa}\right)}$

We proceed to the same kind of identification to match the two models.

$$\dot{E}_1 = \frac{\mathrm{d}E_1}{\mathrm{d}s} = \frac{\mathrm{d}E_1}{\mathrm{d}t}\frac{\mathrm{d}t}{\mathrm{d}s} = \frac{1}{2\kappa\left(1+\frac{\gamma_a}{\kappa}\right)}\left[\frac{1}{\sqrt{2}}\exp\left(i(\gamma_p-\alpha\gamma_a)t\right)\frac{\mathrm{d}E_x}{\mathrm{d}t} + i(\gamma_p-\alpha\gamma_a)E_1\right]$$

$$\frac{1}{\sqrt{2}}\exp\left(i(\gamma_p-\alpha\gamma_a)t\right)\frac{\mathrm{d}E_x}{\mathrm{d}t} = \left[-(\kappa+\gamma_a) - i(\kappa\alpha+\gamma_p) + \kappa(1+i\alpha)(2N+1)\left(1+\frac{\gamma_a}{\kappa}\right)\right]E_1 + \frac{\kappa E_{inj}}{\sqrt{2}}\exp\left[i(2\pi\nu_{inj}+\gamma_p-\alpha\gamma_a)t\right]$$

We obtain :

$$\dot{E}_1 = \frac{1}{2\kappa\left(1+\frac{\gamma_a}{\kappa}\right)}\left[2N(\kappa+\gamma_a) + 2i\alpha N(\kappa+\gamma_a)\right]E_1 + \frac{E_{inj}}{2\sqrt{2}\left(1+\frac{\gamma_a}{\kappa}\right)}\exp\left(i\frac{2\pi\nu_i}{2\kappa\left(1+\frac{\gamma_a}{\kappa}\right)}s\right)$$

$$\dot{E}_1 = N(1+i\alpha)E_1 + \frac{E_{inj}}{2\sqrt{2}\left(1+\frac{\gamma_a}{\kappa}\right)}\exp\left(i\frac{2\pi\nu_i}{2\kappa\left(1+\frac{\gamma_a}{\kappa}\right)}s\right)$$

We can also identify with the model given in [28] :

$$\gamma = \frac{E_{inj}}{2\sqrt{2}\left(1+\frac{\gamma_a}{\kappa}\right)}$$

$$\Delta = \frac{2\pi\nu_i}{2\kappa\left(1+\frac{\gamma_a}{\kappa}\right)}$$

$$\dot{E}_2 = \frac{\mathrm{d}E_2}{\mathrm{d}s} = \frac{\mathrm{d}E_2}{\mathrm{d}t}\frac{\mathrm{d}t}{\mathrm{d}s} = \frac{1}{2(\kappa+\gamma_a)}\left[\frac{1}{\sqrt{2}}\exp\left(-i(\gamma_p-\alpha\gamma_a)\right)\frac{\mathrm{d}E_y}{\mathrm{d}t} - i(\gamma_p-\alpha\gamma_a)E_2\right]$$

$$\frac{1}{\sqrt{2}}\exp\left(-i(\gamma_p-\alpha\gamma_a)\right)\frac{\mathrm{d}E_y}{\mathrm{d}t} = (2N(\kappa+\gamma_a) + 2\gamma_a + i[2N\alpha(\kappa+\gamma_a) + \alpha\gamma_a + \gamma_p])E_2$$

$$\dot{E}_2 = (1+i\alpha)\left(N + \frac{\gamma_a}{\kappa+\gamma_a}\right)E_2$$

We identify the last parameters to obtain the model from [28] :

$$k = 1 \quad \text{and} \quad \beta = -\frac{\gamma_a}{\kappa+\gamma_a}$$

$$\begin{aligned}
\frac{\mathrm{d}E_1}{\mathrm{d}t} &= (1+i\alpha)NE_1 + \gamma\exp(i\Delta t)\\
\frac{\mathrm{d}E_2}{\mathrm{d}t} &= k(1+i\alpha)(N-\beta)E_2\\
T\frac{\mathrm{d}N}{\mathrm{d}t} &= P - N - (1+2N)(|E_1|^2 + |E_2|^2)
\end{aligned}$$

These equations are modified in the same way did in appendix A (the mathematical steps are the same and we do not give them), and we obtain :

$$\begin{aligned} E_1 &= R_1 \exp(i\Delta t + i\phi_1) \\ E_2 &= R_1 \exp(i\phi_2) \end{aligned}$$

$$\begin{aligned} \dot{R}_1 &= NR_1 + \gamma \cos\phi_1 \\ \dot{\phi}_1 &= -\Delta + \alpha N - \frac{\gamma}{R_1}\sin\phi_1 \\ \dot{R}_2 &= k(N-\beta)R_2 \\ T\dot{N} &= P - N - (1+2N)(R_1^2 + R_2^2) \end{aligned}$$

We focus now on the steady-state where both polarizations are excited (IL+PS), given by $\dot{R}_1 = \dot{\phi}_1 = \dot{R}_2 = \dot{N} = 0$ and $R_1, R_2 > 0$. This steady state give :

$$\begin{aligned} N_0 &= \beta \\ \gamma\cos\phi_{1,0} &= -\beta R_{1,0} \\ \gamma\sin\phi_{1,0} &= R_{1,0}(\alpha\beta - \Delta) \\ R_{1,0}^2 + R_{2,0}^2 &= \frac{P-\beta}{1+2\beta} \end{aligned}$$

We can analyse the stability of this solution by studying small perturbations around the steady-state (we note for a variable V : $V_0 + \delta V$ where δV is small. $\delta V_1 \cdot \delta V_2$ become insignificant). We have :

$$\begin{aligned} \delta\dot{R}_1 &= (N_0 + \delta N)(R_{1,0} + \delta R_1) + \gamma\cos(\phi_{1,0} + \delta\phi_1) \\ \delta\dot{\phi}_1 &= -\Delta + \alpha(N_0 + \delta N) - \frac{\gamma}{(R_{1,0} + \delta R_1)}\sin(\phi_{1,0} + \delta\phi_1) \\ \delta\dot{R}_2 &= k((N_0 + \delta N) - \beta)(R_{2,0} + \delta R_2) \\ T\delta\dot{N} &= P - (N_0 + \delta N) - (1 + 2(N_0 + \delta N))((R_{1,0} + \delta R_1)^2 + (R_{2,0} + \delta R_2)^2) \end{aligned}$$

We now expand everything, using linear ordinary differential equations and the steady-state equations. We give the example for $\delta\dot{\phi}_1$, and just the result for the other variables.

$$\begin{aligned} \delta\dot{\phi}_1 &= -\Delta + \alpha(N_0 + \delta N) - \frac{\gamma}{(R_{1,0} + \delta R_1)}\sin(\phi_{1,0} + \delta\phi_1) \\ &= -\Delta + \alpha N_0 + \alpha\delta N - \frac{\gamma}{R_{1,0}\left(1 - \dfrac{\delta R_1}{R_{1,0}}\right)}(\sin(\phi_{1,0})\cos(\delta\phi_1) + \cos(\phi_{1,0})\sin(\delta\phi_1)) \end{aligned}$$

With : $N_0 = \beta$, $\cos(\delta\phi_1) = 1$ and $\sin(\delta\phi_1) = \delta\phi_1$

$$\begin{aligned} \delta\dot{\phi}_1 &= -\Delta + \alpha\beta + \alpha\delta N - \frac{\gamma}{R_{1,0}}\left(1 - \frac{\delta R_1}{R_{1,0}}\right)(\sin(\phi_{1,0}) + \cos(\phi_{1,0})\delta\phi_1) \\ &= \alpha\beta - \Delta - \frac{\gamma}{R_{1,0}}\sin(\phi_{1,0}) + \alpha\delta N - \frac{\gamma}{R_{1,0}}\cos(\phi_{1,0})\delta\phi_1 + \frac{\gamma}{R_{1,0}^2}\sin(\phi_{1,0})\delta R_1 \end{aligned}$$

So : $\delta\dot{\phi}_1 = \dfrac{\alpha\beta - \Delta}{R_{1,0}}\delta R_1 + \beta\delta\phi_1 + \alpha\delta N$

The result for the other variables give the following system, that we can write as a matrix system.

$$\begin{aligned}
\delta\dot{R}_1 &= \beta\delta R_1 + R_{1,0}(\Delta - \alpha\beta)\delta\phi_1 + R_{1,0}\delta N \\
\delta\dot{\phi}_1 &= \frac{\alpha\beta - \Delta}{R_{1,0}}\delta R_1 + \beta\delta\phi_1 + \alpha\delta N \\
\delta\dot{R}_2 &= kR_{2,0}\delta N \\
\delta\dot{N} &= \frac{-2(1+2\beta)}{T}R_{1,0}\delta R_1 - \frac{2(1+2\beta)}{T}R_{2,0}\delta R_2 - \frac{(1+2P)}{T(1+2\beta)}\delta N
\end{aligned}$$

$$\begin{pmatrix}\delta\dot{R}_1\\ \delta\dot{\phi}_1\\ \delta\dot{R}_2\\ \delta\dot{N}\end{pmatrix} = \begin{pmatrix} \beta & R_{1,0}(\Delta-\alpha\beta) & 0 & R_{1,0} \\ \frac{-(\Delta-\alpha\beta)}{R_{1,0}} & \beta & 0 & \alpha \\ 0 & 0 & 0 & kR_{2,0} \\ \frac{-2(1+2\beta)}{T}R_{1,0} & 0 & \frac{-2(1+2\beta)}{T}R_{2,0} & \frac{-(1+2P)}{T(1+2\beta)} \end{pmatrix} \cdot \begin{pmatrix}\delta R_1\\ \delta\phi_1\\ \delta R_2\\ \delta N\end{pmatrix}$$

The stability analysis study the characteristic polynomial of this matrix. We obtain the characteristic polynomial with a formal calculation software. This study is done in the main chapter 2.2.

$$\lambda^4 + a_1\lambda^3 + a_2\lambda^2 + a_3\lambda + a_4 = 0$$

Where :

$$\begin{aligned}
a_1 &= \frac{1+2P}{T(1+2\beta)} - 2\beta \\
a_2 &= \frac{-2\beta}{T}\frac{(1+2P)}{(1+2\beta)} + (\Delta-\alpha\beta)^2 + \beta^2 + \frac{2(1+2\beta)}{T}(R_{1,0}^2 + kR_{2,0}^2) \\
a_3 &= \frac{1}{T}\left[\frac{(1+2P)}{(1+2\beta)}((\Delta-\alpha\beta)^2+\beta^2) + 2(1+2\beta)\left[(\alpha(\Delta-\alpha\beta)-\beta)R_{1,0}^2 - 2k\beta R_{2,0}^2\right]\right] \\
a_4 &= \frac{2kR_{2,0}^2}{T}(1+2\beta)((\Delta-\alpha\beta)^2+\beta^2)
\end{aligned}$$

According to [28], the conditions for the stability of the steady state are given by the Routh-Hurwitz conditions :

$$a_1 > 0, \quad a_3 > 0, \quad a_4 > 0, \quad a_1a_2a_3 - a_3^2 - a_1^2a_4 > 0$$

C Delayed Bifurcation

In this appendix, we give some precisions about delayed bifurcations. This phenomenon appears when crossing "slowly" a bifurcation. The study of the phenomenon has been made for a laser with a time dependent parameter [38], and to understand qualitatively the phenomenon, we will study the works [43] and [44], even if the models in these papers are much simpler than the one we are working with in this document (the spin-flip model).

In this simpler model for a class A laser, the transverse field for the single-mode is given by the expression :

$$\dot{E} = aE - B|E|^2E + \xi(t)$$

Where $\xi(t)$ is the spontaneous emission noise. We can define the power $I = |E|^2$, and we have the following :

$$\dot{I} = 2\left(E\frac{\mathrm{d}E^\star}{\mathrm{d}t} + E^\star\frac{\mathrm{d}E}{\mathrm{d}t}\right) = 2(a - BI)I$$

$$\text{The steady} - \text{state} \ : \ \dot{I} = 0 \quad \Rightarrow \quad I = \frac{a}{B} \ \text{ or } \ I = 0$$

$$\text{We can define} \ : \ \dot{I} = -\frac{\mathrm{d}U(I)}{\mathrm{d}I} \quad \text{(Potential well)}$$

$$U(I) = -aI^2 + \frac{2B}{3}I^3$$

The steady state can be modelled by figure C.1 where the dashed line ($I = 0$) is unstable for positive values of a and $I = a/B$ is stable for positive values of a.

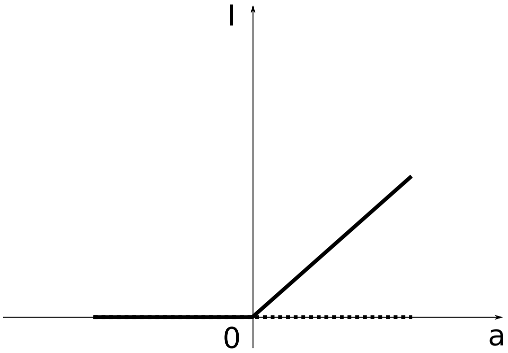

Figure C.1: $I = f(a)$. a is a time dependent parameter - Dashed line is an unstable state and continuous line is the stable state

In this model, the parameter a is time dependent ($a = vt$) as shown in figure C.2. In this figure, we show the potential well $U(I)$ at different times (t_1 to t_4), and the position of the "ball" that model if $I(t)$ reach the steady-state of the potential well.

If the system would reach the steady-state instantaneously, the steady-state would be the dashed line of figure C.3 described by :

$$I = \frac{a(t)}{B} = \frac{vt}{B}$$

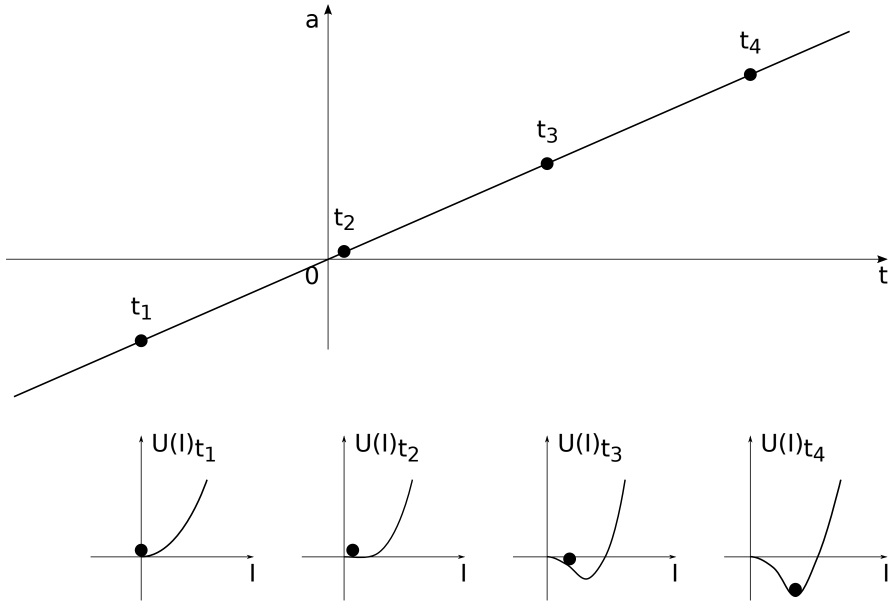

Figure C.2: Delayed bifurcation explained for a simple model of potential well, and only one time dependent parameter (a)

However for small values of the parameter a, the system does not reach the steady-state (the "balls" in the potential wells of figure C.2) and we have a delay as shown in figure C.3, where t_1 to t_4 are the one defined on figure C.2.

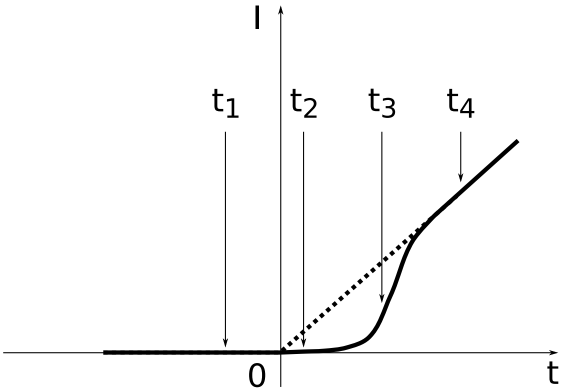

Figure C.3: Delayed bifurcation explained for a simple model. I reach the steady-state after a delay. The instantaneous steady-state is the dashed line

In our work, the model is much more complicated, but qualitatively, the phenomenon can be described the same way. In our work, the time dependent parameter is the injected power of the master laser in the optical injection process.

D List of Publications

The stay at the *Instituto de fisica de Cantabria* has led to some publication work. Most of them are not published yet, but only submitted. We give here the list of the work, and a copy of the different papers.

1. Polarization Switching and Injection Locking in 1550nm VCSELs Subject to Parallel Optical Injection

Authors : A. Quirce, P. Pérez, A. Popp, F. Denis-le Coarer, A. Valle, L. Pesquera, Y. Hong, H. Thienpont, K. Panajotov, and M. Sciamanna

Journal : ISLC 2016 Conference Paper

2. Analysis of the Polarization of a VCSEL Subject to Parallel Optical Injection

Authors : A. Quirce, A. Popp, F. Denis-le Coarer, P. Pérez, A. Valle, L. Pesquera, Y. Hong, H. Thienpont, K. Panajotov, and M. Sciamanna

Journal : Submitted to *Physical Review E*

3. Polarization Non-Linear Dynamics of a VCSEL Subject to Parallel Optical Injection

Authors : F. Denis-le Coarer, Ana Quirce, A. Valle, L. Pesquera, M. Sciamanna, H. Thienpont, and K. Panajotov

Journal : Submitted to *Optics Express*

4. Injection Locking and Polarization Switching Bistability in a 1550nm-VCSEL Subject to Parallel Optical Injection

Authors : F. Denis-le Coarer, Ana Quirce, P. Pérez, A. Valle, L. Pesquera, M. Sciamanna, H. Thienpont, and K. Panajotov

Journal : Submitted to *Journal of the Optical Society of America B*

5. Experimental Polarization Nonlinear Multistability and Coherence Intermittency in a VCSEL Subject to Parallel Optical Injection

Authors : F. Denis-le Coarer, Ana Quirce, A. Valle, L. Pesquera, M. Sciamanna, H. Thienpont, and K. Panajotov

Journal : Intended for submission to *Physical Review A*